Investigation of Low-Speed Turbulent Separated Flow Around Airfoils

A. J. Wadcock

TURBULENT SEPARATED FLCW ARCUND AIRFOILS
(Analytical Methods)   66 p   CSCL 01A

                                                          Unclas
                                               G3/02   0111703

NASA

Investigation of Low-Speed Turbulent Separated Flow Around Airfoils

A. J. Wadcock
Analytical Methods, Inc.
Redmond, Washington

NASA

National Aeronautics and
Space Administration

Ames Research Center
Moffett Field California 94035

TABLE OF CONTENTS

ABSTRACT

The present report documents a low-speed wind tunnel experiment to measure the flowfield around a two-dimensional airfoil operating close to maximum lift. Boundary layer separation occurs on the upper surface at $x/c=0.85$. A three-component laser velocimeter. coupled with a computer-controlled data acquisition system, was used to obtain three orthogonal mean velocity components and three components of the Reynolds stress tensor in both the boundary layer and wake of the airfoil. Pressure distributions on the airfoil. skin friction distribution on the upper surface of the airfoil. and integral properties of the airfoil boundary layer are also documented. In addition to these "near field" flow properties, static pressure distributions, both upstream and downstream from the airfoil and on the walls of the wind tunnel. are also presented.

iii

ACKNOWLEDGEMENTS

1. INTRODUCTION

Considerable progress has been made in the ability to compute the flow field around complex geometries provided that the interaction between the boundary layer on the body and the external inviscid flow is relatively weak. For boundary layer effects to be adequately accounted for in such calculations the relevant Reynolds number must be large and the boundary layer (either laminar or turbulent) must remain attached almost everywhere. Under such conditions aerodynamic design capability is extremely good. A logical long-term extension to this capability is the development of methods for predicting flow fields containing extensive regions of flow separation. Trailing-edge stall of a two-dimensional airfoil serves both as a natural starting point for such a study and a logical step in the advancement of design methods for conventional unswept wings and high-aspect-ratio helicopter blades.

Whilst knowledge of $C_{L_{max}}$ is important for airfoils developed for fixed-wing aircraft, an increase in $C_{L_{max}}$ is also desirable in order to improve the performance of the blade tip on rotor craft. On a rotor, the angle of incidence, Mach number, and local sweep all fluctuate with time, and there is a centrifugal force acting on the rotor-blade boundary layer. Helicopter rotor performance both in hover and at forward speed can be computed using a quasi-steady approach when the downwash variation over the disk due to the periodic vortex wake created by the rotor in earlier revolutions is taken into account. Steady two-dimensional section characteristics are stored in the computer as reference data, though modifications such as assuming that C_L remains constant at incidences above the stall are often made in order to improve the correlation between measured and calculated rotor performance. Thus considerable emphasis is placed on the accurate knowledge of $C_{L_{max}}$ over a wide range of Mach number in two-dimensional flow.

Information gained from experiment is often a necessary step in the development of computational methods used to solve complex flows. The present experiment was performed to provide information that will assist the development and testing of such methods. The NACA 4412 airfoil section was chosen for study because it has a gradually increasing region of separation with increase in angle-of-attack rather than an abrupt leading-edge stall (Reference 1).

Considerable difficulty is often encountered in obtaining a fully two-dimensional steady stalled condition. Gregory *et al* (Reference 2) observed that at high angles of incidence the flow in the corner between the airfoil and the tunnel walls is inclined to separate before the flow over the center of the model, thus destroying two-dimensionality across the span. Corner separation can be suppressed by boundary layer control on both the tunnel wall and the airfoil close to the wall. Gregory *et al* used single slots in the tunnel walls ahead of the airfoil and a perforated airfoil surface close to the end-walls. As the chordwise extent of separation grows with increasing angle of incidence, the separation

becomes three-dimensional in character. This development is unaffected by treatment of the corner flow. This three-dimensionality shows up as curvature of the separation line and pronounced spanwise flow. If the separation point moves forward from the airfoil trailing-edge at one local spanwise position, with consequent loss of lift, the trailing vortices on each side of this initially stalled region induce an upwash between them and a downwash outboard, thus stabilizing a "stall cell"of span less than the model span. A strong stall cell can induce sufficient downwash to suppress corner separation.

Oil flow studies by Winkelmann *et al* (References 3 and 4) have shown such patterns to exist not only on full-span or 2-D rectangular wings in the vicinity of stall but also on stalled finite aspect ratio wings free from any direct wall interference. For aspect ratios above 3 it was shown that multiple stall cells exist in the early stages of wing stall which eventually merge into one large cell at higher angles of attack.

Coles and Wadcock (Reference 5) employed several forms of boundary layer control on the end walls without success. Careful placement of vortex generators on the tunnel walls. however. were used with excellent results. The requirement of optical access to the airfoil boundary layer eliminated this method of flow control by Hastings *et al* (References 6 and 7). Instead. multiple fences distributed across the span of the airfoil were used successfully. The spanwise positions of the fences were found to be critical. as were the positions of their fixing brackets if they were near the leading-edge suction peak.

Measurements in separated flow fields are difficult to make for a variety of reasons. In particular, separated flows tend to be very sensitive to the insertion of probes and their supports. and the use of pressure probes or conventional hot-wire anemometry in regions of flow reversal or high turbulence intensity suffer from difficulties in interpreting such data. Coles and Wadcock (Reference 5) avoided one of the above problems. that of directional ambiguity associated with conventional hot-wire anemometry. by mounting a hot wire on the end of a rotating arm. More recently, Hastings *et al* (References 6 and 7) and Wadcock[*] used a two-component LV as the primary measurement instrument. employing frequency-shifting by Bragg cells to overcome difficulties associated with mean flow reversals and high turbulence levels.

Hastings used a two-component. photon-correlation laser Doppler anemometer oper-ated in back-scatter. and encountered little difficulty in making measurements of mean ve-locity. Problems encountered in the measurement of turbulence. however. were attributed to the poor signal-to-noise ratio available from back-scatter operation and to difficulties with stable co-alignment at long range (2.7-metres). To compensate for the absence of reliable turbulence data from the LV. Hastings used a stationary hot wire for turbulence measurements. Hot wire turbulence measurements however were not presented for the

---

[*] Wadcock. A.J.. "Two-component Laser Doppler Anemometer Measurements in the Near Wake of a Stalled Airfoil."unpublished work. October. 1985.

inner third of the boundary layer due to rectification of the hot wire signal. Wadcock used a two-component high-resolution boundary layer LV operated in back-scatter with a distinct disadvantage from Hastings' arrangement ..... the two anemometer channels were non-orthogonal and closely-coupled (see Orloff and Olson, Reference 8, for details of the LV). Lack of success in obtaining reliable turbulence data was similarly attributed to poor signal-to-noise ratio from the LV operated in back-scatter at large range. The highly-coupled nature of the non-orthogonal channels also made turbulence measurements very sensitive to noise on either channel. This high-resolution LV had a very small focal volume ($60\mu m$ dia.) at an operating range of 2.5-metres, and a change of 2 degrees C in ambient temperature in the vicinity of the optical table would cause complete misalignment of the beams. Continual realignment was therefore essential.

The present investigation makes use of a 3-D LV described in detail by Snyder *et al* (Reference 9) and Orloff *et al* (Reference 10). Two orthogonal channels measure the streamwise and cross-stream velocity components, U and W, directly. The spanwise velocity component, V, is measured indirectly from a non-orthogonal coupling with the cross-stream velocity component W. The arrangement of the transmitting optics is such that alignment is very stable and is not sensitive to thermal changes of the environment. The measuring volume is approximately 0.012in. diameter. This is much larger than for the high-resolution boundary layer LV, but as the boundary layer is almost 4.5 inches thick at the airfoil trailing-edge this is not critical.

2.   EXPERIMENTAL DETAILS

2.1.   WIND TUNNEL

The experiment was performed in the 7 ft. by 10 ft. wind tunnel (7 × 10 No.2) at NASA Ames Research Center. Moffett Field, California. The facility is a conventional closed circuit wind tunnel with a working section 15 ft. in length. The working section height is constant at 7 ft., and its width varies linearly from an initial value of 10 ft. to a final value of 10.1335 ft. in order to allow for boundary layer growth. There are no turbulence-reducing screens in the wind tunnel circuit, and recent measurements by Soderman (Reference 11) in an almost identical companion tunnel (7 × 10 No.1) indicate test section turbulence levels of $u'/U = 0.0025, v'/U = w'/U = 0.0085$ for the chosen test conditions.

2.2.   MODEL

The airfoil model is fabricated of fiberglass-reinforced polyester resin with a highly polished surface. The model is composed of two pieces - a main body and a full-span hatch cover. The hatch extends from $x/c=0.18$ to $x/c=0.73$ on the pressure surface providing access to the interior for installation of ribs. spars, and pressure instrumentation. The airfoil has an NACA 4412 section and constant chord of 90 cm. This is the same model used for the studies reported in References 5 and 8.

Use of the three-component LV dictated that the model be mounted horizontally in the tunnel in order that the velocity components of importance. U and W, were measured directly by the two orthogonal channels. In order to span the full width of the test section the original model span of 78.4 inches was increased by the addition of identical 21-inch extensions rigidly attached to each end of the instrumented central section. The model was supported from the floor of the tunnel by means of a pair of steel plates welded to the tunnel floor. and adjacent overlapping steel plates protruding from the pressure surface on the inboard end of each extension (see Figures 1 and 5). These plates were aligned with the axis of the tunnel and allowed discrete changes in the angle of attack by simply selecting appropriate bolt holes in each plate.

The pitch pivot-point was located outside the airfoil section at $(x/c, z/c) = (0.250, -0.169)$ in airfoil coordinates. 1.418 chords downstream of the start of the test section and 0.239 chords below the tunnel axis. Thus at $\alpha = 0$ the chordline is approximately 2.5 inches below the tunnel centerline. The wing-wall intersection was sealed by means of felt pads at the wing tips to eliminate leakage around the model ends. To ensure uniform transition across the span. boundary layer trips were mounted on both upper and lower surfaces of

the airfoil. Each trip had a width of 0.22in., a thickness of 0.007in. and a sawtooth leading-edge. The suction-surface trip was centered at $x/c = 0.023$ and the pressure-surface trip at $x/c = 0.10$.

The model was instrumented with 200 static pressure taps. 66 of which were distributed chordwise at the mid-span of the airfoil. Two additional chordwise rows of 56 orifices each are located approximately 1/2-chord on each side of the semi-span location. In addition to these chordwise rows, a spanwise row of 22 upper-surface orifices is located at the 0.25-chord position. The static pressure at these 200 static-pressure orifices was measured using five internally mounted 48-port scanivalves equipped with 1.0-psi pressure transducers. The chordwise pressure distributions so obtained were numerically integrated to obtain the section force and moment coefficients C_L, C_D and C_M.

2.3. INSTRUMENTATION

In addition to airfoil surface pressure measurements as outlined above, tunnel roof and floor pressure measurements were made using a sting-mounted pitot-static tube. This probe could be positioned anywhere in the test section using the wind tunnel traverse. which gains access to the test section through two streamwise slots in the tunnel roof close to the sidewalls. Vertical surveys were also performed at the mid-span location both upstream and downstream from the airfoil. The same traverse was used to position a sting-mounted pitot-rake on the airfoil in order to document the attached suction-side boundary layer inaccessible to the LV. In order to quantify the displacement effect of the wind tunnel boundary layer, pitot-rake measurements were made on both the roof and floor of the test section at the airfoil trailing-edge location.

The main instrument used for the study of the airfoil boundary layer and wake was a three-component LV described in detail in References 10 and 9. The optical table was mounted on a traverse mechanism situated just outside the tunnel as shown in Figure 1. Vertical and streamwise motion of the test point are accomplished by moving the entire optical table on a digitally controlled platform. Optical encoder readback to the stepper-motor controllers ensures location accuracy. The system software is highly interactive and special data acquisition. reduction, and display programs have been written to ensure that the data is of good quality. For example, during data acquisition. histograms and population statistics are displayed on the graphics terminal. simultaneously for all 3 channels. so that immediate information is available to the engineer. The lower set of rails are yawed slightly with respect to the tunnel axis. and the optical table is pitched downwards a similar amount (2.74 degrees). to allow grazing contact of the focal volume at the semi-span of the wing. Three velocity components are measured by means of three independent dual-scatter channels that operate in backscatter. The two strongest colors (514.5-nm green line and 488.0-nm blue line) from a 4-Watt argon-ion laser provide a coupled measurement of the on-axis velocity component V. For an optical table that is neither pitched nor yawed.

the 514.5-nm green line and the 476.5-nm violet line sense the cross-stream (vertical) and streamwise (horizontal) velocity components W and U directly. The small pitch and yaw angle of the optical table in the present configuration results in a slight coupling of all 3 velocity components .... no velocity component is measured directly.

Backscatter velocimeters are subject to an inherently poor signal-to-noise ratio (SNR). As the SNR is inversely proportional to the processing bandwidth, it follows that the SNR can be enhanced by minimizing the bandwidth. However, if the bandwidth is too narrow, the incoming data may be biased by the bandpass filter if (a) the mean frequency moves to the edges of the bandpass as the velocity varies during a survey, or (b) the turbulence intensity is high enough to cause the distribution of frequencies to extend beyond one or both edges of the bandpass. To alleviate this problem, the 3-D LV system incorporates programmable frequency synthesizers (Orloff *et al*, Reference 10) that generate, for each channel, a mixer frequency that can be varied under program control so as to maintain the mean signal frequency (as seen by the counter processor) at the center of the band-width. In this way, the SNR is improved because a minimum bandwidth may be adopted. Also, at a constant signal frequency, the counter processor accuracy remains constant. Frequency shifting by Bragg cells is employed to resolve directional ambiguity in the measured velocities.

A characteristic of non-orthogonal LV systems is that the computed orthogonal velocity components may exhibit high systematic uncertainties. Orloff and Snyder (Reference 12) and Snyder, Orloff and Reinath (Reference 13) performed an uncertainty analysis and error estimation for the present LV geometry. Their studies led to the development by Snyder [*] of an advanced LV calibration technique. The calibration technique employs 5-μm wires mounted on a spinning disc and can produce a velocity accurate to 0.1 percent in magnitude and 0.1 degrees in direction. The calibration-disc is easy to use, very repeatable from day to day, and now plays an essential role in the use of the 3-D LV.

The 3-D LV was originally designed to provide mean velocity data only (all 3 components) and operate in zoom. However, for the measurement of turbulence in all 3 directions, and turbulent correlations in particular, there is the additional requirement of simultaneity on all 3 channels. This requires that all 3 channels see the same particle at nearly the same time. All 3 focal points must then be coincident in space. This would be difficult to achieve while operating in zoom. Hence, for this experiment, the 3-component LV was operated in *fixed – focus* mode, allowing measurements only in a single plane close to the semi-span of the airfoil. A benefit of operating in fixed-focus mode is that the LV calibration is much more accurate than for zoom operation and also less time consuming. The requirement of simultaneity on all three channels reduces the data rate dramatically, extending the time

---

[*] Snyder, P.K., "Calibration of a 3-D LDA using a velocity reference source," to be published.

required to achieve a desired population (typically 1000 samples which might take from 2 to 5 minutes). This severely reduces the number of data points obtained and velocity scans possible in the time available.

The laser was operated at a power setting of typically 1.5 to 2 Watts (all colors). With 1.5 Watts total laser power, the power in each green beam was found to be 65mW. The power in the green beams is twice the power in the blue beams and four times the power in the violet beams. The effective probe volume for each channel was initially found to be of length $L_{green} = L_{violet} = 0.2$ inch, $L_{blue} = 0.1$ inch, with beam waist diameters $d_{green} = d_{blue} = d_{violet} = 0.012$ inch. Beam expanding lenses (magnification power $\times 3$) were inserted into the two orthogonal channels (ahead of the beamsplitter-Bragg cell assembly) in order to tighten the focus, increase the beam intensity at the focus and hence improve the signal-to-noise ratio (at the expense of a possible problem with long range alignment). New values for the focal volume size were not determined.

Counter cycle-time was delayed to prevent multiple readings from the same particle, and all LV data have been corrected for sampling bias using the correction appropriate for a spherical focal volume (Johnson *et al*, Reference 14).

The air stream was seeded with atomised mineral oil droplets introduced at the downstream end of the tunnel test section. The LV boundary layer and wake surveys were always obtained along lines normal to the local wing surface and to the free stream direction respectively.

3. TEST CONDITIONS

The primary aim of the present investigation was to obtain LV measurements in a two-dimensional separated mean flow. The mean flow above a stalled airfoil can depart significantly from the plane two-dimensional ideal (see Winkelmann, Reference 4). Obtaining an acceptable approximation to plane mean flow can be a time consuming task. Following Hastings et al (Reference 7), streamwise fences running around the leading edge of the wing and continuing along the upper surface to $x/c = 0.494$ were installed between the original 6.5-ft. span model and the dummy extensions. thereby shielding the central instrumented section from the tunnel wall boundary layer. All mounting hardware for the fences was recessed as recommended by Hastings. Each fence was manufactured in short segments. contoured to the local airfoil curvature. If a particular section of fence was removed. it was replaced by a metal strap whose outside surface was flush with the local airfoil surface.

An initial study involved tufting the complete upper surface of the airfoil with white yarn and observing flow patterns for a range of angle of attack. Figure 2 shows a photograph corresponding to $\alpha = 12$ degrees. Flow is from top to bottom in the figure. To provide increased contrast between the model and the tufts. illumination was obtained by suspending an ultraviolet source above the wing at the mid-span location. Tufts in the attached boundary layer are relatively steady. but immediately start to "cone" as separation is approached and the turbulence level rises. The apparent reduction in tuft motion each side of mid-span is a result of non-uniform intensity of illumination. Tufts in the last three rows can be seen to spend a significant fraction of the time pointing upstream. The position for which that fraction of time is 50% is defined to be the mean separation point (solely for the purpose of quantifying the tuft study). The results of this initial study are presented in Figure 3 and illustrate the relatively smooth. but rapid. upstream motion of the separation point with increasing angle of attack. Note that a 1 degree change in angle of attack will move the separation point a long way - typically 15 percent of the chord.

A geometric angle of attack of 12 degrees was chosen for the LV study based on separation location (from observations of wool-tufts) and from spanwise uniformity of surface pressure distributions. Above this angle of attack. unsteadiness increased rapidly leading to irregularity in the spanwise pressure distribution. The undisturbed free-stream velocity for the tests was 29.1m/s. The corresponding Mach number was 0.085 and Reynolds number based on airfoil chord 1.64 $\times$ 10^6. Additional surface pressure data were taken on the airfoil to define the lift curve in the vicinity of $C_{L_{max}}$.

The airfoil deflection under load at the test conditions was measured optically at the semi-span. This motion was found to be composed of a vertical translation of the airfoil trailing-edge of 0.009in. (upwards in the tunnel) accompanied by a nose-up rotation of 0.025 degrees.

4. EXPERIMENTAL RESULTS

4.1. WIND TUNNEL BOUNDARY CONDITIONS

The present experiment is performed in a facility where optical access dictates the streamwise location of the model. Unfortunately, this places the model sufficiently far upstream to allow the pressure signature of the airfoil on the tunnel walls to reach the tunnel static plate. Static pressure measurements made along the tunnel center-line using a sting-mounted pitot-static tube attached to the wind tunnel traverse, close to the roof and floor of the test section, are shown in in Figure 4. These pressure distributions should be helpful in calculations of the displacement effect of the tunnel wall boundary layer, and measured values for the displacement thickness are given at a single streamwise station above and below the airfoil trailing-edge. The pressure signature on the tunnel walls extends upstream into the contraction cone (beyond the tunnel static plate), and downstream into the diffuser. It is clear that nowhere in the 15-ft. long test section does the static pressure return to its undisturbed value. The result of a vertical traverse both upstream and downstream from the airfoil is shown in Figure 5. The upstream traverse can be used to determine an initial onset velocity distribution at that station because the total head is constant across the duct ahead of the airfoil (measurements of total head at this station showed no systematic gradient across the tunnel within the accuracy of the measurements, 0.0025 in C_{p_t}). However, this is not recommended because two-dimensionality of the static pressure field ahead of the airfoil was not verified experimentally. The upstream static pressure distribution results from the complete three-dimensional pressure distribution across the airfoil span and may not be simply related to the locally two-dimensional conditions existing at mid-span. The data are included here simply to illustrate the far-reaching pressure signature of the airfoil. Note that the same observation applies to the measured tunnel-wall pressure distributions. This data, however, is only to be used for estimating the tunnel wall boundary layer displacement effect, which is itself a second order effect.

The same figure shows the locations of the pressure orifices of the static plate on each side-wall. By definition, C_p at the static plate is zero. Clearly, the vertical pressure distribution measured at semi-span is not the same as the side-wall pressure distribution. Close to the side-walls the airfoil section lift coefficient is reduced from that at mid-span, and so we would expect a somewhat reduced cross-stream static pressure gradient ahead of the airfoil at that spanwise location.

A few more words about tunnel interference are worthwhile. The original investigation (Reference 5) was performed in the Caltech 10-ft. diameter wind tunnel which has a rather short test section of length 10 feet i.e., test-section length diameter = 1. Although wall pressure measurements were not made in that facility it is immediately obvious from Figure 4 that a more serious problem would have existed if the tunnel static plate had

been used to define free-stream static pressure and free-stream velocity on that occasion. The circular cross-section was not well suited for the study of a two-dimensional flow and so a two-dimensional test section was created by the insertion of a pair of parallel false walls. The leading edge of this insert extended upstream into the contraction cone and the trailing-edge extended downstream into the diffuser. The static-plate orifices, therefore, lay outside the two-dimensional insert and were deemed inappropriate to define free-stream conditions. Instead, all pressures and velocities were non-dimensionalized with those measured at a convenient reference position close to the airfoil, inside of the two-dimensional insert. The position chosen is of little significance (provided the coordinates are supplied) as it is assumed, from the outset, that anybody wishing to compute such a flowfield would necessarily have to include the tunnel walls.

Boundary layers on both roof and floor at the airfoil trailing-edge location were measured with the airfoil at 12 degrees angle of attack. Data for the roof boundary layer are as follows: $\delta = 4.6$in., $\delta^* = 0.49$in., $\theta = 0.38$in. and $C_f = 0.00250$. Corresponding data for the floor boundary layer are $\delta = 4.8$in., $\delta^* = 0.57$in., $\theta = 0.45$in. and $C_f = 0.00245$. Relevant velocity information at these two positions can be obtained from the tunnel-wall pressure data presented in Figure 4.

4.2.   AIRFOIL SURFACE PRESSURE DISTRIBUTION

Pressure distributions around the airfoil at 3 spanwise locations are shown in Figure 6 for a range of angle of attack at a nominal Reynolds number of 1.64×10^6 . The existence of separation on the upper surface of the airfoil can be recognized by the appearance of a constant pressure region that spreads rapidly upstream from the trailing edge with increasing angle of attack. Increased scatter in the pressure distributions and increased non-uniformity across the span become evident above $\alpha = 12$ degrees. Corresponding force coefficient data are presented in Figure 7 from which it is evident that the airfoil is operating close to maximum lift at $\alpha = 12$ degrees. Surface pressure distributions at α 12 degrees corresponding to $Re_c = 1.21 \times 10^6$ and $Re_c = 2.31 \cdot 10^6$ are shown in Figures 8 and 9. Figure 10 illustrates the sensitivity of airfoil section coefficients close to maximum lift with change in Reynolds number. Repeatability in surface pressure data is ± 0.01 in C_p. apart from the immediate vicinity of the leading-edge suction peak. for all α less than or equal to 12 degrees.

A comparison of Hastings measured pressure distribution at $\alpha = 12.15$ degrees with the present data at α 12 degrees is shown in Figure 11. Also shown are the Caltech data for $\alpha = 13.87$ degrees. The latter data have been adjusted according to $C_p = 0.8553C_{p_{r,f}} - 0.1447$ based on the measured tunnel floor pressure distribution of Figure 4 assuming a similar degree of wall interference for the two geometries. It is clear that all 3 surface pressure distributions are essentially the same and it would therefore be expected that the corresponding velocity and turbulence data would agree likewise.

Although the geometric angle-of-attack for the Caltech study was 13.87 degrees it is apparent from the present study that the effective angle of incidence was closer to 12 degrees. A possible explanation may be that the short working-section (length/diameter = 1) of the Caltech wind tunnel causes the test-section to behave like a venturi, with streamline curvature in the test section accounting for the large change in effective angle-of-attack.

4.3.   PITOT-RAKE MEASUREMENTS IN THE BOUNDARY LAYER

Mean velocity profiles were measured at mid-span in the airfoil boundary layer for angles of attack 12 and 13 degrees using a sting-mounted pitot-rake supported from the tunnel traverse. These measurements were made in order to provide data in the upstream part of the attached boundary layer, inaccessible to the LV because of limited streamwise travel of the optical table. Boundary layer velocities have been inferred by assuming constant static pressure through the boundary layer equal to the local airfoil surface pressure. Ahead of separation, the boundary layer is thin and this assumption is good. As separation is approached and the boundary layer thickens, this assumption is less valid, but under these conditions the total pressure measurement itself is also suspect because of increased turbulence levels.

Figure 12(a) shows measurements of boundary layer growth on the upper surface of the airfoil for $\alpha=12$ degrees. Note the increased growth rate for $\delta_{0.995}$ as separation is approached. Note also the measurements for $\alpha=13$ degrees showing that separation has moved much further upstream. Pitot rake measurements of $\delta_{0.995}$ are, of course, valid both upstream and downstream of separation, but suffer from the fact that the boundary layer thickness is difficult to measure with great accuracy. Integral boundary layer parameters such as displacement thickness δ and momentum thickness θ can be measured with much greater reliability, and this data is presented in Figures 12(b) and 12(c). Pitot-rake measurements for δ and θ are increasingly suspect as separation is approached, but data for the initial attached boundary layer should be reliable. Excellent agreement is obtained between the present pitot-rake measurements for δ (restricted to pre-separation for obvious reasons), Hastings' LV measurements and the Caltech FHW (flying hot wire) measurements all the way to the trailing edge. Once again, data for $\alpha=13$ degrees is shown for comparison. It would appear from Figure 12(c) that the momentum thickness θ is a more sensitive measure than δ of any differences that may exist between the three experiments. Comparison of momentum thickness measurements between all three datasets is quite good up to separation but thereafter the agreement is less satisfactory, for no obvious reason.

A similar comparison for shape factor $H = \delta / \theta$ between the three datasets is shown in Figure 12(d). It should be noted that H=4 is often associated with fully separated mean flow.

11

Figure 13 represents estimates of local skin friction coefficient, $C_f = 2\tau_w/\rho U_e^2$, from Clauser plots of mean velocity. The present pitot-rake data blend smoothly into the Caltech FHW measurements (which indicate separation at x/c=0.85) . Hastings' measurements indicate slightly earlier separation which may be related to higher initial values for θ on the suction-side of the airfoil.

The pitot-rake was also used to document the boundary layer on the pressure-side of the airfoil near the trailing-edge. For x/c=0.978 the following measurements were obtained: $\delta \simeq 0.75$in., $\delta^* \simeq 0.052$in., $\theta = 0.041$in. and $C_f \simeq 0.00461$.

4.4. LV MEASUREMENTS IN THE BOUNDARY LAYER AND WAKE

LV boundary layer measurements on the upper airfoil surface are presented in Figures 14, 15 and 16 at x/c=0.529, 0.815 and 0.952 respectively. The first station is upstream of separation, the second is close to separation and the third station is downstream of separation. Wake data is presented in Figures 17 and 18 at x_w/c=0.007, immediately downstream of the airfoil trailing edge, and a short distance downstream at $x_w/c = 0.282$ respectively. Boundary layer profiles were measured along local normals to the airfoil surface; wake profiles were measured along normals to the tunnel axis. The upper surface velocity profiles have been integrated to yield the displacement and momentum thicknesses and shape factor $H = \delta^*/\theta$. This information is included in Figure 12 alongside the pitot-rake data.

Measurements of the spanwise mean velocity component indicate that V is generally 4% or less of U_e in both the boundary layer and wake, although occasional measurements indicate higher values. Measurements of V show more scatter than the direct measurements of U and W and illustrate the increased uncertainty associated with a coupled measurement from two non-orthogonal channels. Of more significance is the growth of V with downstream distance. At x/c=0.529 both positive and negative values for V are encountered through the boundary layer, although the tendency is for V to be negative. At all subsequent stations the spanwise mean velocity component V is negative throughout the layer indicating streamline divergence from the plane of measurement.

Insufficient LV data are available from the present study to pinpoint the separation point accurately. However, separation clearly occurs downstream of the second boundary layer station at x/c=0.815. Hastings LV measurements indicate separation at x/c=0.80 whereas the Caltech FHW (flying-hot-wire) data indicate separation at x/c=0.85. (A partial listing of the Caltech FHW data at selected stations in the boundary layer and wake is available in Reference 15. In this reference, all velocities are resolved normal and parallel to the airfoil *chordline*. Data are tabulated every 5cm along the chord for $0.62 \leq x/c \leq 1.29$ (every 10cm for $1.29 \leq x/c \leq 1.84$) and every 0.2cm normal to the chord. The same data is presented in conventional boundary layer coordinates (velocities

resolved normal and parallel to the local airfoil surface) in Reference 16 in the form of contour plots.

Present measurements of reversed flow velocity indicate a maximum value of $-0.16U_e$ at x/c=0.952, slightly higher than Hastings' measurements and the Caltech dataset which both indicate $-0.13U_e$, but the disagreement is certainly within the bounds of experimental uncertainty. From Figure 16, at x/c=0.952 the reverse-flow region occupies the inner 25% of the boundary layer in the mean (although intermittent backflow occurs throughout the inner 2/3 of the layer). This compares with values of 29% from Hastings and 23% from the Caltech dataset at the trailing edge.

The mean velocity component normal to the airfoil surface, W, is seen to grow rapidly with downstream distance. The no-slip condition, of course, forces $W = 0$ at the airfoil surface. At the edge of the boundary layer however, $(W/U)_e$ is seen to grow from 3% at x/c=0.529, to 18% at x/c=0.815 and 22% at x/c=0.952. The small change in $(W/U)_e$ between x/c=0.815 and x/c=0.952 indicates there is, initially, very little change in shear layer direction after the boundary layer separates. Clearly the boundary layer assumption $W << U$ is invalid in this region. Indeed, boundary layer coordinates are not necessarily desirable once separation has occurred and the shear layer has detached from the airfoil surface. A more useful coordinate system might be aligned with the shear layer.

Hastings found that all normal Reynolds stresses were suppressed to their free-stream values beyond $n/\delta=0.75$ due to curvature effects, and that the dominant shear stress term, $\overline{u'w'}$, was negligible outside of $n/\delta=0.6$. The present LV data show no suppression of turbulence in the outer part of the boundary layer; nor does the Caltech data (References 17 and 18). At the first station, x/c=0.529, the maximum value for $\overline{u'u'}$ is reached close to the wall. Not surprisingly, the maximum for $\overline{w'w'}$ occurs further out in the layer due to the damping effect of the wall. Estimates for C_f from $\overline{u'w'}$ measured close to the wall agree reasonably well with Clauser plot estimates from the mean velocity. At x/c=0.815 the peak in $\overline{u'u'}$ has increased considerably. This peak is located close to the region of maximum mean rate of strain $\partial U/\partial n$. The Reynolds shear stress, not unexpectedly has its maximum value where both normal stresses reach their maxima.

The Caltech FHW (flying hot wire) data show values for u'/U_e above 0.28 and present LV data reach $u'/U_e \approx 0.35$ whereas Hastings *stationary* hot wire data only indicate maximum values of $u'/U_e \approx 0.17$. The disagreement is easily explained. Hastings discarded certain hot wire data on the basis of comparison between mean velocity measured with the hot wire and that measured using the LV. Reynolds stresses were only presented for parts of the boundary layer where the techniques yielded mean velocity profiles "of very similar shape". Examination of the mean velocity profile at x/c=0.952 shown in Figure 16(a) in conjunction with the distribution of γ_{nu} (the fraction of LV samples having a negative value for U) shown to the right, illustrates the problem. Note that in the middle of the layer 20% of the LV measurements indicate reverse-flow. Figure 16(b) indicates

13

that both normal stresses, $\overline{u'u'}$ and $\overline{w'w'}$, peak at about the same location in the layer. Hastings presents *stationary* hot wire data for $n/\delta \geq 0.5$ that are, therefore, more than likely subject to significant rectification effects and will therefore indicate lower turbulence levels under such conditions. Unfortunately Hastings provides no turbulence data in the wake. We shall see later that at $x_w/c = 0.282$ γ_{nu} is zero across the entire wake and, thus, the stationary hot wire could be expected to provide reliable information, and a valid comparison between the datasets could have been made at this station.

Although the suppression of turbulence in the outer part of the boundary layer was not indicated by either the Caltech (FHW) data or the present (LV) data, another feature of strongly curved flows was evident. At the first station for which LV data is available, $x/c=0.529$. Figure 14(b) shows that the correlation $\overline{u'w'}$ is negative throughout the layer as expected. The correlation attains its maximum value some distance from the wall as expected for a boundary layer in an adverse pressure gradient (see Simpson *et al*, Reference 17). At the next station for which LV data is available, $x/c=.815$, the boundary layer is very close to separating as shown by the mean velocity profile in Figure 15(a), and data for γ_{nu} indicate that intermittent separation has already occured at this station. The Reynolds shear stress distribution through the layer has changed significantly as shown in Figure 15(b). The $\overline{u'u'}$ correlation is very weak close to the wall, but assumes a strong positive value in the outer part of the boundary layer. This result is not totally unexpected. Gillis and Johnston (Reference 18) studied the effect of strong convex curvature on boundary layer turbulence. Their flow passed from a flat surface, over a convex surface with 90° of turning, to a flat recovery surface with zero pressure gradient along the test surface. At the introduction of curvature, the shear stress in the outer part of the layer was sharply diminished. In a distance of about 3 boundary-layer thicknesses the shear stress in the outer 70% of the boundary layer had disappeared completely. This was followed by the appearance of a region of negative turbulent shear stress (positive $\overline{u'u'}$) in the outer part of the layer. The appearance of this region of negative shear stress was explained by examination of the transport equation for Reynolds-stress in a curved boundary layer. The process of recovery from curvature was found to be very much slower than the initial response to the start of curvature. Clearly, in the case of airfoil stall, with $\delta/R \approx 0.01$ at $x/c=0.6$ increasing to $\delta/R \approx 0.03$ at $x/c=0.85$. we have two competing effects. First, streamwise convex curvature tends to suppress turbulence levels and can produce negative shear stress in the outer part of the layer. Second, the increased turbulent activity associated with the approach to separation apparently more than compensates for the suppression due to curvature. and large negative values for the shear stress are encountered in the outer part of the layer. From Figure 16(b). at $x/c=0.952$. we find that $(\overline{u'w'}/U_e^2)_{max}$ ≈ 0.014 with $\overline{u'w'}/\sqrt{u'^2}\sqrt{w'^2} \approx +0.5$. These values are somewhat higher than measured with the flying hot wire but the two datasets agree qualitatively.

LV measurements in the wake are presented in Figures 17 and 18. Note that all wake

measurements are presented in tunnel coordinates. Measurements of mean velocity in the wake show the thin shear layer originating from the pressure side of the airfoil and the much thicker layer coming from the suction surface. For $\alpha=12$ degrees the surface slope, in tunnel coordinates, at the airfoil trailing-edge is given by $\partial z/\partial x=-0.21$ for the pressure surface and -0.52 for the suction surface. If the flow remains parallel to the local airfoil surface we would expect the ratio W/U to assume the same values just downstream of the airfoil trailing-edge on either side of the wake. The boundary layer remains attached on the airfoil pressure surface and we would therefore expect the ratio W/U to approach the value -0.21 underneath the wake. The measurements shown in Figure 17(a) are in reasonable agreement. For the suction surface, in the absence of separation, we would similarly expect W/U to approach -0.52 above the wake. However, since the flow no longer follows the upper surface of the airfoil it is not surprising that the measured cross-stream velocities are much lower.

The Caltech dataset indicates that the reverse-flow region extends downstream from the airfoil trailing edge to $x_w/c = 0.07$ with maximum reverse-flow velocity 13 percent of U_∞, after which the two shear layers merge into an asymmetric wake. This is in good agreement with Hastings LV measurements of mean velocity which indicate closure of the separation bubble at $x_w/c = 0.09$. The present LV measurements indicate slightly higher values for the reverse-flow velocity as indicated earlier.

Each shear layer has a peak in both $\overline{u'u'}$ and $\overline{u'w'}$ associated with it. This is evident from the wake traverse at $x_w/c = 0.007$ shown in Figure 17(b). Note that the locations of these peaks closely match the points of inflection in the mean velocity profile shown in Figure 17(a). The normal stress maxima occuring in the pressure-surface shear layer are smaller than those in the suction-surface shear layer. The turbulent shear stress correlation $\overline{u'w'}$ reaches large values in regions of high mean shear $\partial U/\partial z$, separated by a region where $\overline{u'w'}$ is low and the mean velocity gradient is also small.

At the second wake station, $x_w/c = 0.282$, the two shear layers appear to have merged and only a single peak in both $\overline{u'u'}$ and $\overline{u'w'}$ exists as shown in Figure 18(b). Notice the rapid approach to isotropy that takes place between $x_w/c = 0.007$ and $x_w/c = 0.282$. At the downstream station, only two boundary-layer thicknesses downstream of the airfoil trailing-edge, the turbulence is essentially isotropic.

15

5. CONCLUSIONS AND RECOMMENDATIONS

The present study validates and augments an extensive dataset (References 5, 15 and 16), obtained by use of the flying hot-wire, documenting the boundary layer and near wake of an airfoil operating at maximum lift. The present flowfield measurements were made using a three-component laser velocimeter. Test conditions were chosen so as to establish a surface pressure distribution on the airfoil almost identical to that reported in Reference 5. Measurements were compared with the above dataset and with data from a similar LV investigation by Hastings *et al* (References 6 and 7). Mean velocity measurements from all 3 studies show good agreement. Hastings *et al* were unable to obtain reliable turbulence measurements from the LV and used a *stationary* hot wire to measure turbulence in the outer part of the boundary layer. These measurements are believed to be contaminated by rectification of the hot wire signal. Comparison of the present turbulence measurements is therefore restricted to the Caltech FHW dataset. Both studies indicate very similar values for both $\overline{u'u'}$ and $\overline{w'w'}$. The two techniques, very different in approach and execution, both indicate a region of negative shear stress (positive $\overline{u'w'}$) in the outer part of the boundary layer that first appears some distance upstream of separation.

It is evident from the present study that the tunnel walls must be included in any attempt to compute such a flow. The boundary layer displacement effect on these walls, however, will be of second order. Airfoil stall is a very complex phenomena involving boundary layer growth under the influence of both strong streamwise curvature and strong adverse pressure gradient. In addition to being able to handle boundary layer separation, numerical computations must be able to relax the no-slip boundary condition at the airfoil trailing-edge and model the merging of two greatly different shear layers in order to accurately predict the flow in the wake. With these observations in mind it makes sense to validate a proposed turbulence model by testing the model in a series of flows each of which have only one of the above features present at any time. For example, a possible sequence could be the computation of

(i) a fully attached turbulent boundary layer in *zero pressure gradient with strong streamwise curvature*: comparison with the data of Gillis and Johnston (Reference 18); test case 0233, 1980-81 Stanford Conference on Complex Turbulent Flows.

(ii) separating turbulent boundary layer in an adverse pressure gradient on a flat wall (i.e., no streamwise curvature); comparison with the data of Simpson *et al* (Reference 17); test case 0431, 1980-81 Stanford Conference on Complex Turbulent Flows.

(iii) trailing-edge flow with turbulent boundary layer separation: comparison with the data of Thompson and Whitelaw (Reference 19).

and, finally

16

(iv) airfoil stall - turbulent boundary layer separation from the upper surface of the airfoil under the influence of a strong adverse pressure gradient and strong streamwise curvature; comparison with the present LV data, Hastings LV data (References 6 and 7) and the Caltech FHW data (References 5, 15 and 16); test case 0441, 1980-81 Stanford Conference on Complex Turbulent Flows.

6. REFERENCES

1. Abbott, I.H. and von Doenhoff, A.E., Theory of Wing Sections, Dover Publications, 1959.

2. Gregory, N., Quincey, V.G., O'Reilly. C.L. and Hall, D.J., "Progress Report on Observations of Three-Dimensional Flow Patterns obtained during Stall Development on Aerofoils, and on the Problem of Measuring Two-Dimensional Characteristics," Aeronautical Research Council CP 1146, 1971.

3. Winkelmann, A.E. and Barlow, J.B.. "Flowfield Model for a Rectangular Planform Wing beyond Stall," AIAA Journal Volume 18, page 1006. 1980.

4. Winkelmann, A.E., "Flow Field Surveys of Separated Flow on a Rectangular Planform Wing," AIAA 19th Aerospace Sciences Meeting, St. Louis, Missouri, January 12-15, 1981.

5. Coles, D. and Wadcock, A.J., "Flying-hot-wire Study of Two-dimensional Mean Flow Past a NACA4412 Airfoil at Maximum Lift," AIAA Journal, Volume 17, April 1979.

6. Hastings, R.C. and Williams, B.R.. "Studies of the Flow Field near an NACA 4412 Aerofoil at nearly Maximum Lift," Aeronautical Journal, Volume 91, pp. 29-44. January 1987.

7. Hastings. R.C., Moreton, K.G. and Clark, R.. "Mean flow properties measured around an aerofoil close to its maximum lift," Paper 14-1 2nd. Int. Symposium on Applications of Laser Anemometry to Fluid Mechanics, Lisbon, July 2-4 1984.

8. Orloff. K.L. and Olson, L., "High-resolution LDA measurements of Reynolds Stress in Boundary Layers and Wakes," AIAA 11th Aerodynamic Testing Conference. Colorado Springs, Colorado. March 18-20, 1980.

9. Snyder, P.K.. Orloff, K.L. and Aoyagi. K., "Performance and Analysis of a Three-Dimensional Nonorthogonal Laser Doppler Anemometer," NASA TM 81283, July. 1981.

10. Orloff, K.L., Snyder, P.K. and Reinath. M.S.. "Laser Velocimetry in the Low-Speed Wind Tunnels at Ames Research Center." NASA TM 85885. January, 1984.

11. Soderman, P.T., "Turbulence Measurements in the 7- by 10-foot Wind Tunnel No. 1." NASA Large-Scale Aerodynamics Branch. FSA TM 19. April 27. 1979.

12. Orloff. K.L. and Snyder. P.K.. "Laser Doppler anemometer measurements using nonorthogonal velocity components: error estimates." Applied Optics. Volume 21, page 339. January 15. 1982.

13. Snyder. P.K.. Orloff. K.L. and Reinath. M.S.. "Reduction of Flow-Measurement Uncertainties in Laser Velocimeters with Nonorthogonal Channels." AIAA 21st Aerospace Sciences Meeting, Reno, Nevada. January 10-13. 1983.

14. Johnson, D.A., Modarress, D. and Owen, F.K., "An Experimental Verification of Laser-Velocimeter Sampling Bias and its Correction,"Journal of Fluids Engineering, Volume 106, March 1984.

15. Wadcock, A.J.. "Structure of the Turbulent Separated Flow Around a Stalled Airfoil,"NASA CR 152263, 1979.

16. Wadcock, A.J., "Simple Turbulence Models and Their Application to Boundary Layer Separation,"NASA CR 3283, May 1980.

17. Simpson, R.L., Chew, Y.-T. and Shivaprasad, B.G., "The structure of a separating turbulent boundary layer. Part 1. Mean flow and Reynolds stresses,"JFM, Volume 113, 1981.

18. Gillis, J.C. and Johnston. J.P.. "Turbulent boundary-layer flow and structure on a convex wall and its redevelopment on a flat wall,"JFM. Volume 135,1983.

19. Thompson, B.E. and Whitelaw. J.H.. "Characteristics of a trailing-edge flow with turbulent boundary-layer separation,"JFM. Volume 157. 1985.

7. LIST OF FIGURES

12. Measurements of boundary layer shape parameters.

    12a. $\delta_{0.995}$

    12b. $\delta^{'}$

    12c. θ

    12d. $H = \delta^{'}/\theta$

13. Local skin friction coefficient estimated from Clauser plot of mean velocity.

14. LV measurements in the boundary layer at $x/c = 0.529$.

    14a. Measurements of mean velocity at $x/c = 0.529$.

    14b. Turbulence measurements at $x/c = 0.529$.

15. LV measurements in the boundary layer at $x/c = 0.815$.

    15a. Measurements of mean velocity at $x/c = 0.815$.

    15b. Turbulence measurements at $x/c = 0.815$.

16. LV measurements in the boundary layer at $x/c = 0.952$.

    16a. Measurements of mean velocity at $x/c = 0.952$.

    16b. Turbulence measurements at $x/c = 0.952$.

17. LV measurements in the wake at $x_w/c = 0.007$.

    17a. Measurements of mean velocity at $x_w/c = 0.007$.

    17b. Turbulence measurements at $x_w/c = 0.007$.

18. LV measurements in the wake at $x_w/c = 0.282$.

    18a. Measurements of mean velocity at $x_w/c = 0.282$.

    18b. Turbulence measurements at $x_w/c = 0.282$.
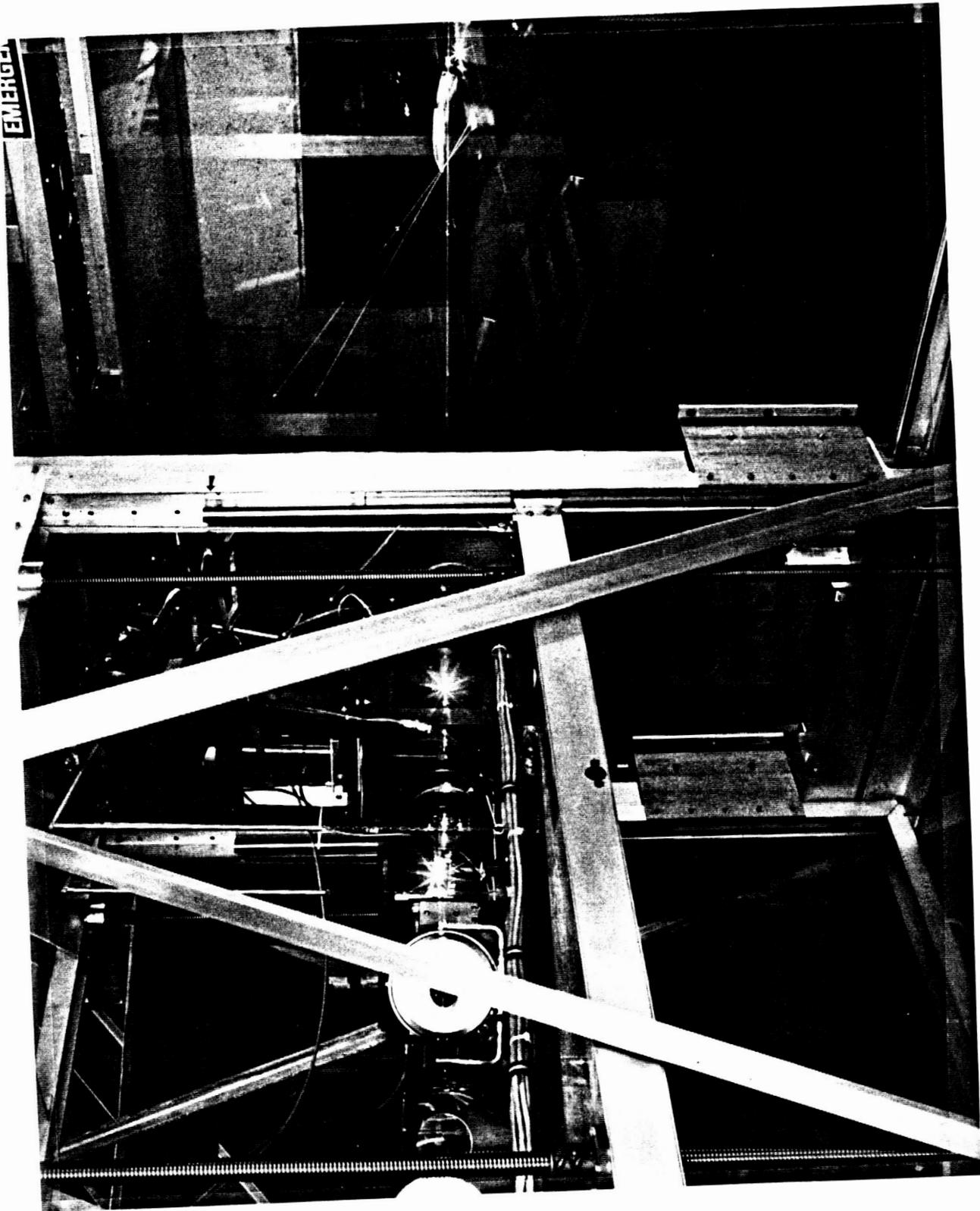
Figure 1. Photograph of model installation in Army 7×10 wind tunnel.
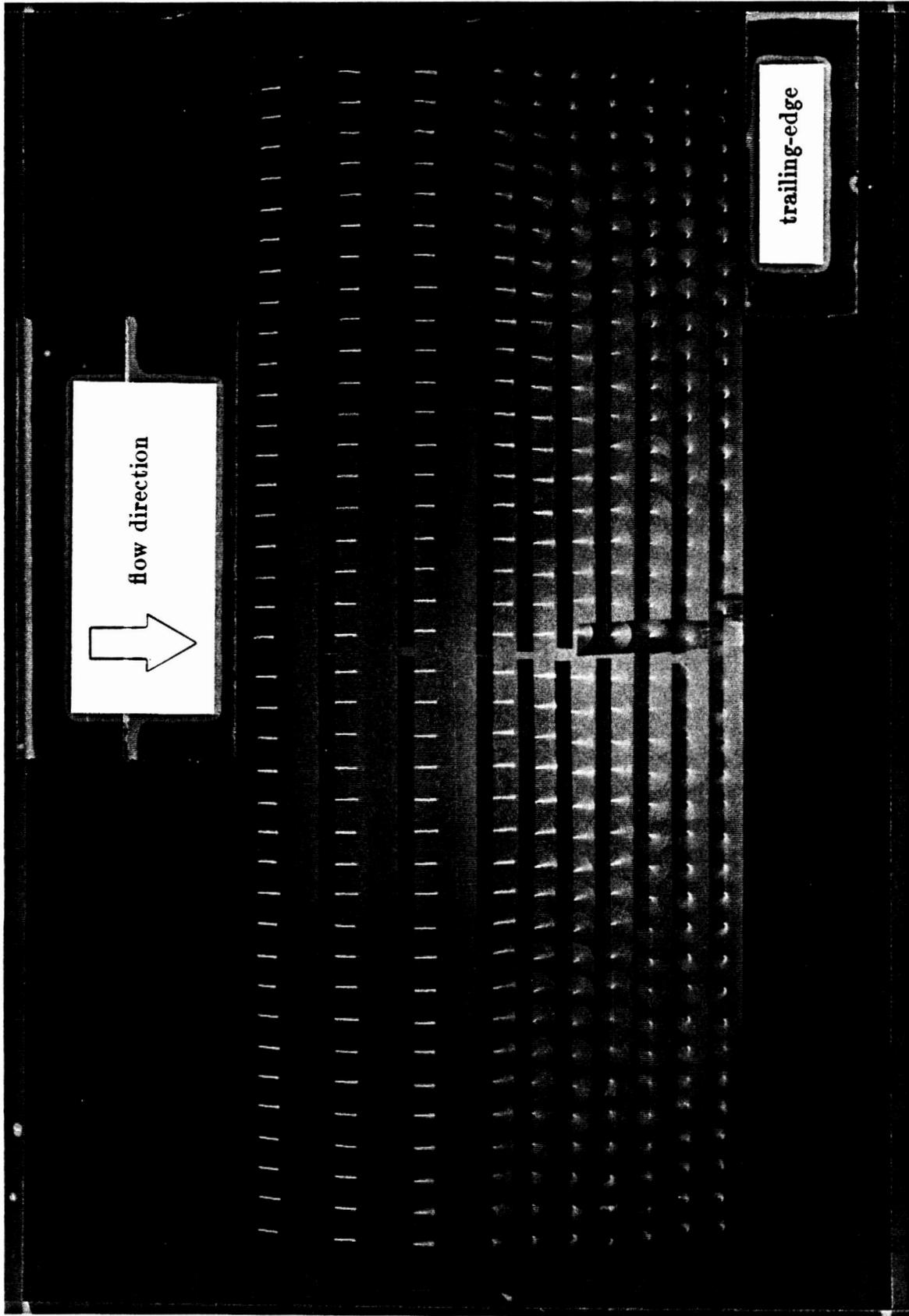
Figure 2. Flow visualization photograph using wool tufts; $\alpha = 12$ degrees.
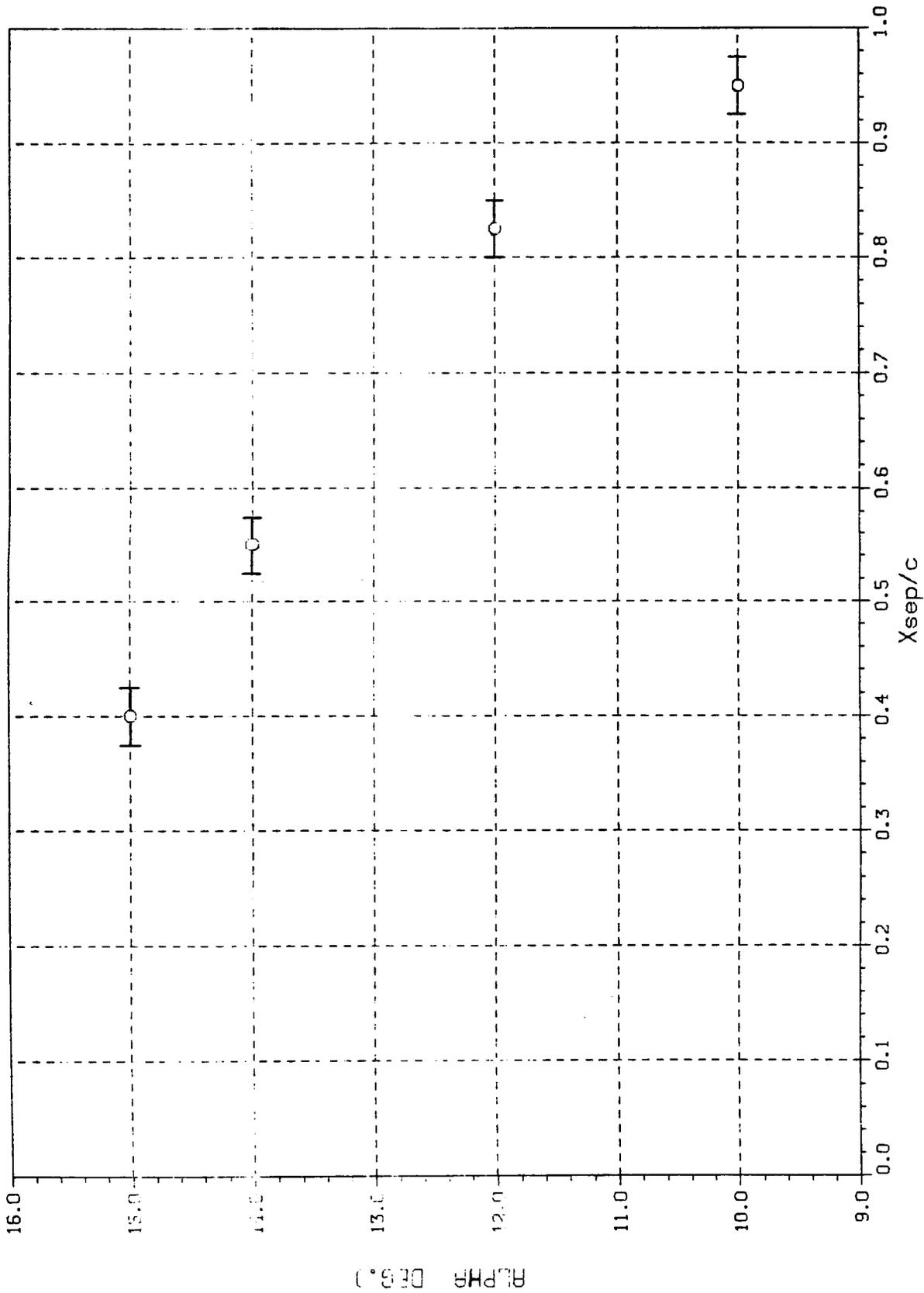
Figure 3. Movement of separation point with angle of attack.

(from observation of wool tufts).

24
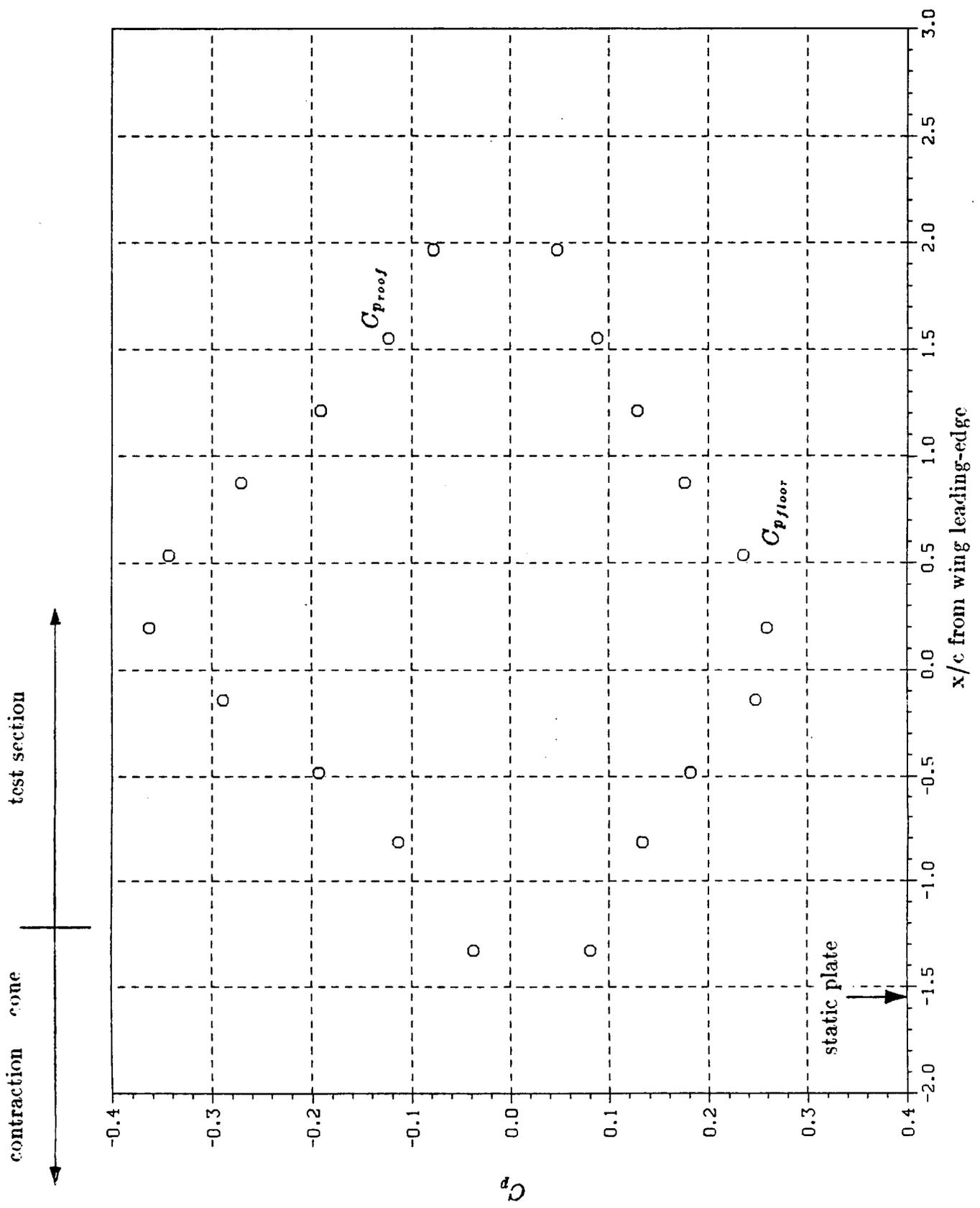
Figure 4. Tunnel wall pressure measurements.

7.00'

15.00'

airfoil coordinates

wake coordinates

n z

z_w

z

x

z

Pivot Point

static-plate orifice location
(both side-walls)

FLOW

B

A

3.00

3.00

C_p
Station B

C_p
Station A
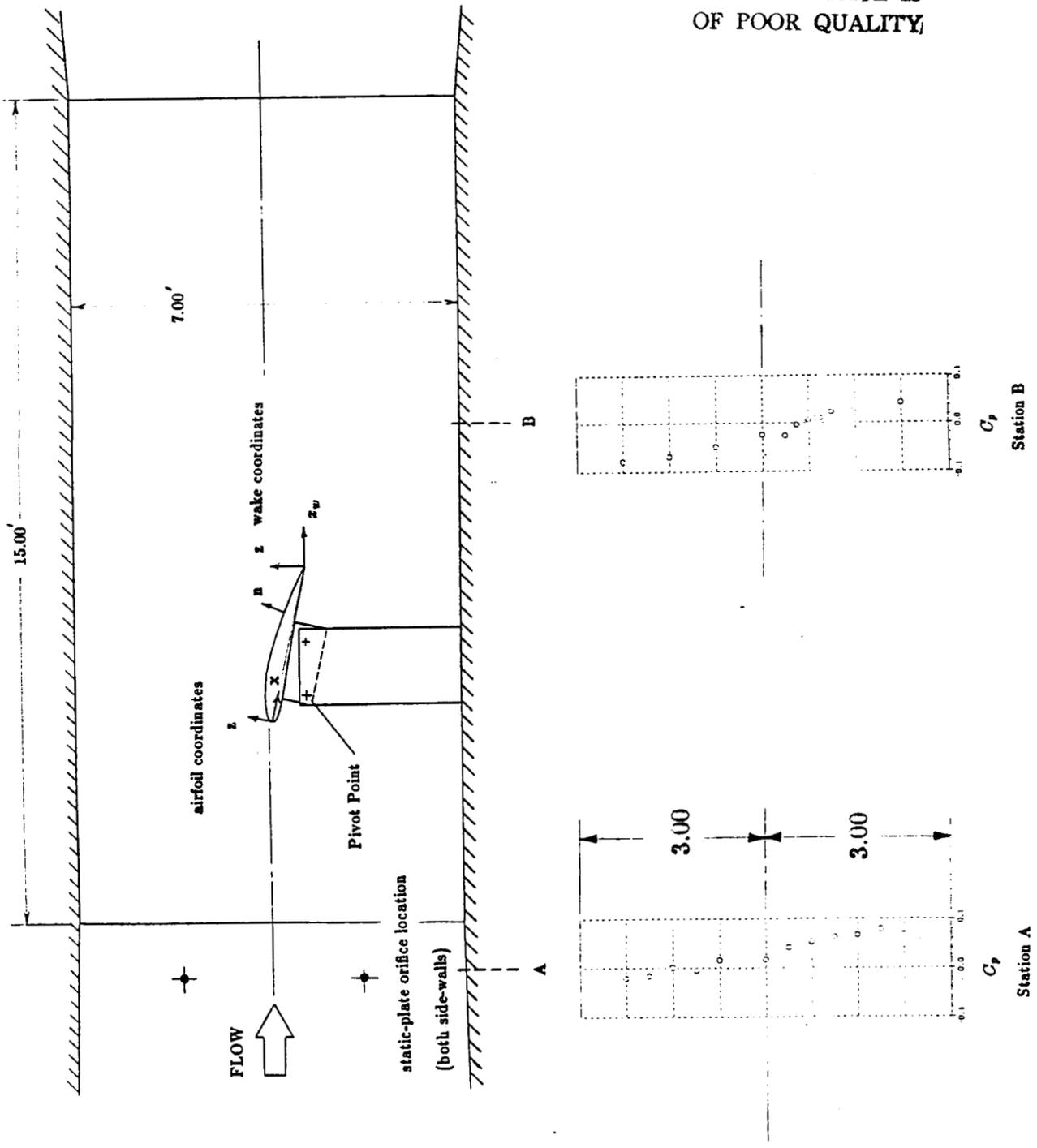
Figure 5. Static pressure surveys upstream and downstream from airfoil.
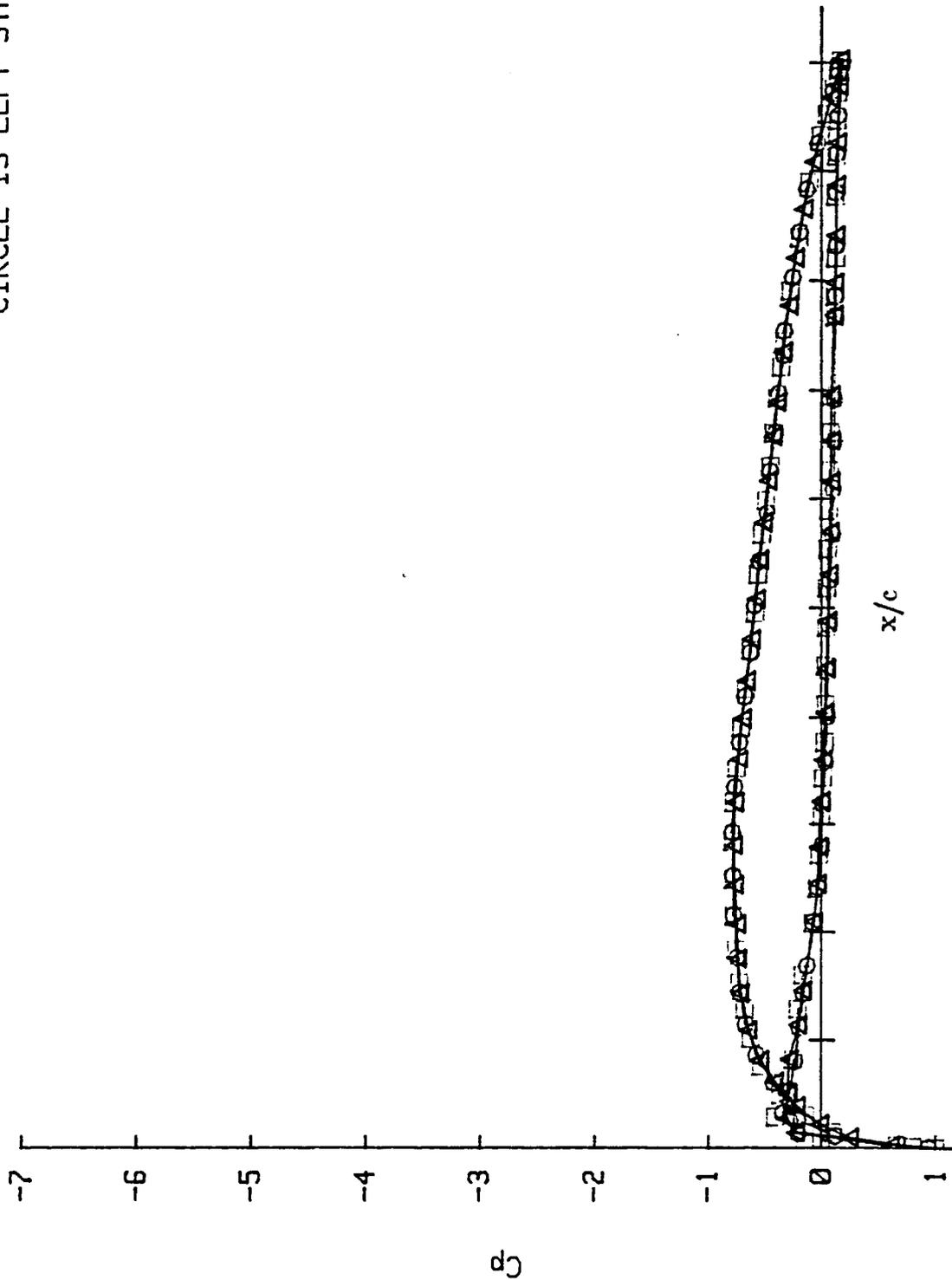
Figure 6a. Airfoil pressure distribution for $Re_c = 1.66 \times 10^6$; $\alpha = 0$ degrees.

27

Figure 6b. Airfoil pressure distribution for $Re_c = 1.64 \times 10^6$; $\alpha = 4$ degrees.

28

RUN 27 POST TEST PLOT OF AVERAGE Cp vs. X/C

TRIANGLE IS RIGHT STATION
SQUARE IS MIDDLE STATION
CIRCLE IS LEFT STATION

Figure 6c. Airfoil pressure distribution for $Re_c = 1.59 \times 10^6$; $\alpha = 8$ degrees.

29

RUN 19 POST TEST PLOT OF AVERAGE Cp vs. X/C

TRIANGLE IS RIGHT STATION
SQUARE IS MIDDLE STATION
CIRCLE IS LEFT STATION
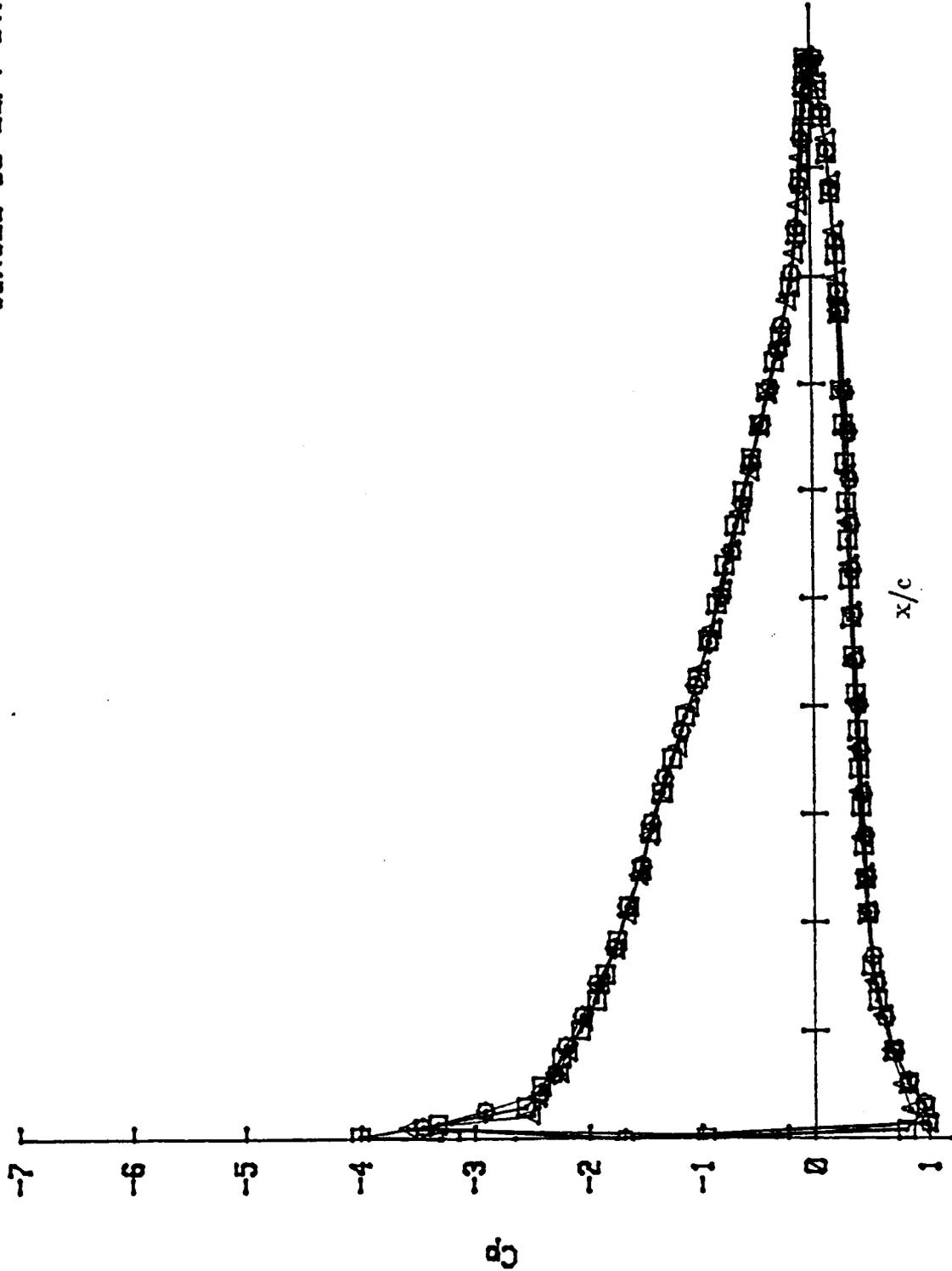
Figure 6d. Airfoil pressure distribution for $Re_c = 1.67 \times 10^6$; $\alpha = 10$ degrees.

RUN 31 POST TEST PLOT OF AVERAGE Cp vs. X/C

TRIANGLE IS RIGHT STATION
SQUARE IS MIDDLE STATION
CIRCLE IS LEFT STATION
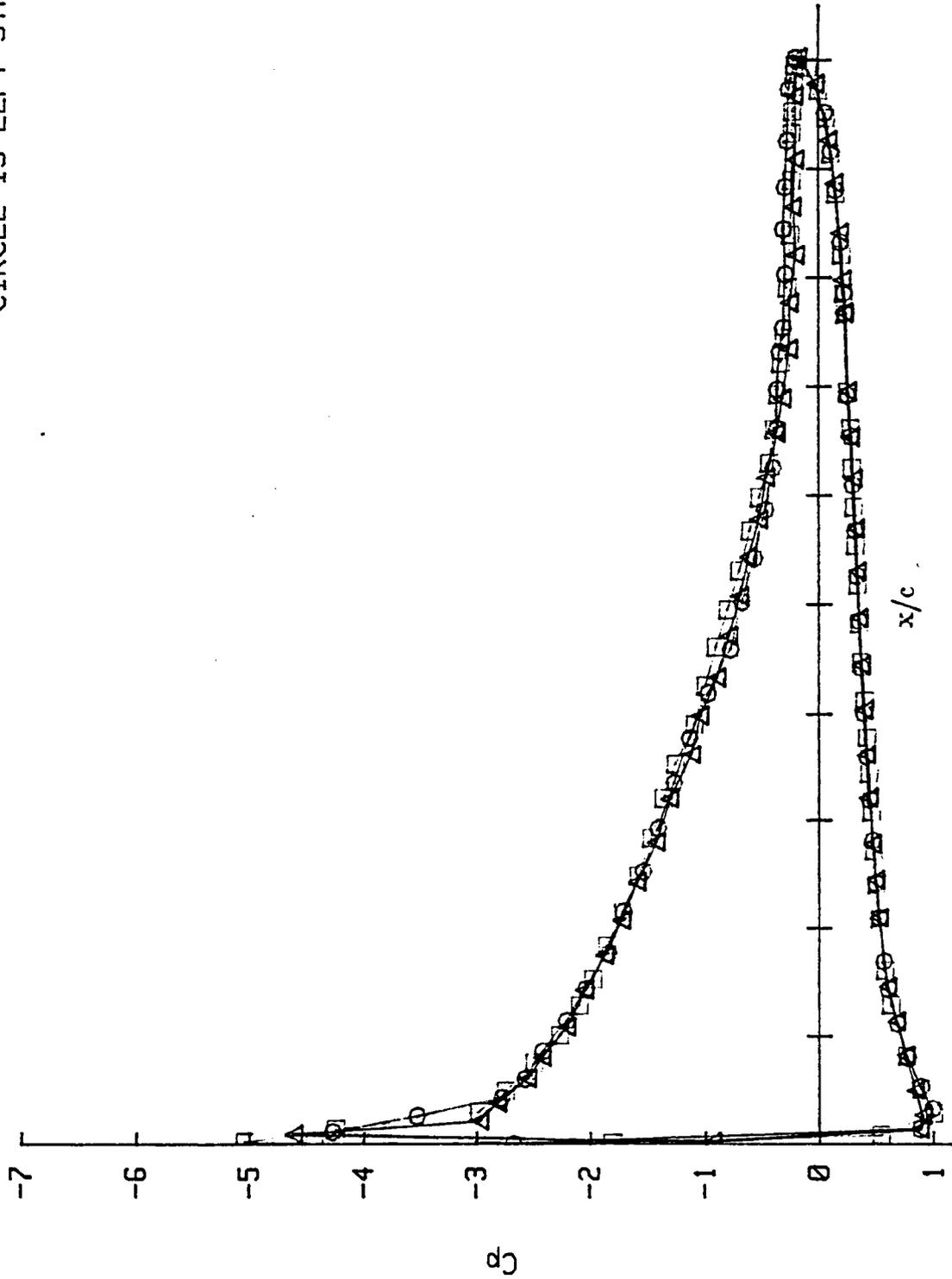
Figure 6e. Airfoil pressure distribution for $Re_c = 1.65 \times 10^6$; $\alpha = 12$ degrees.

TRIANGLE IS RIGHT STATION
SQUARE IS MIDDLE STATION
CIRCLE IS LEFT STATION

RUN 32 POST TEST PLOT OF AVERAGE Cp vs. X/C
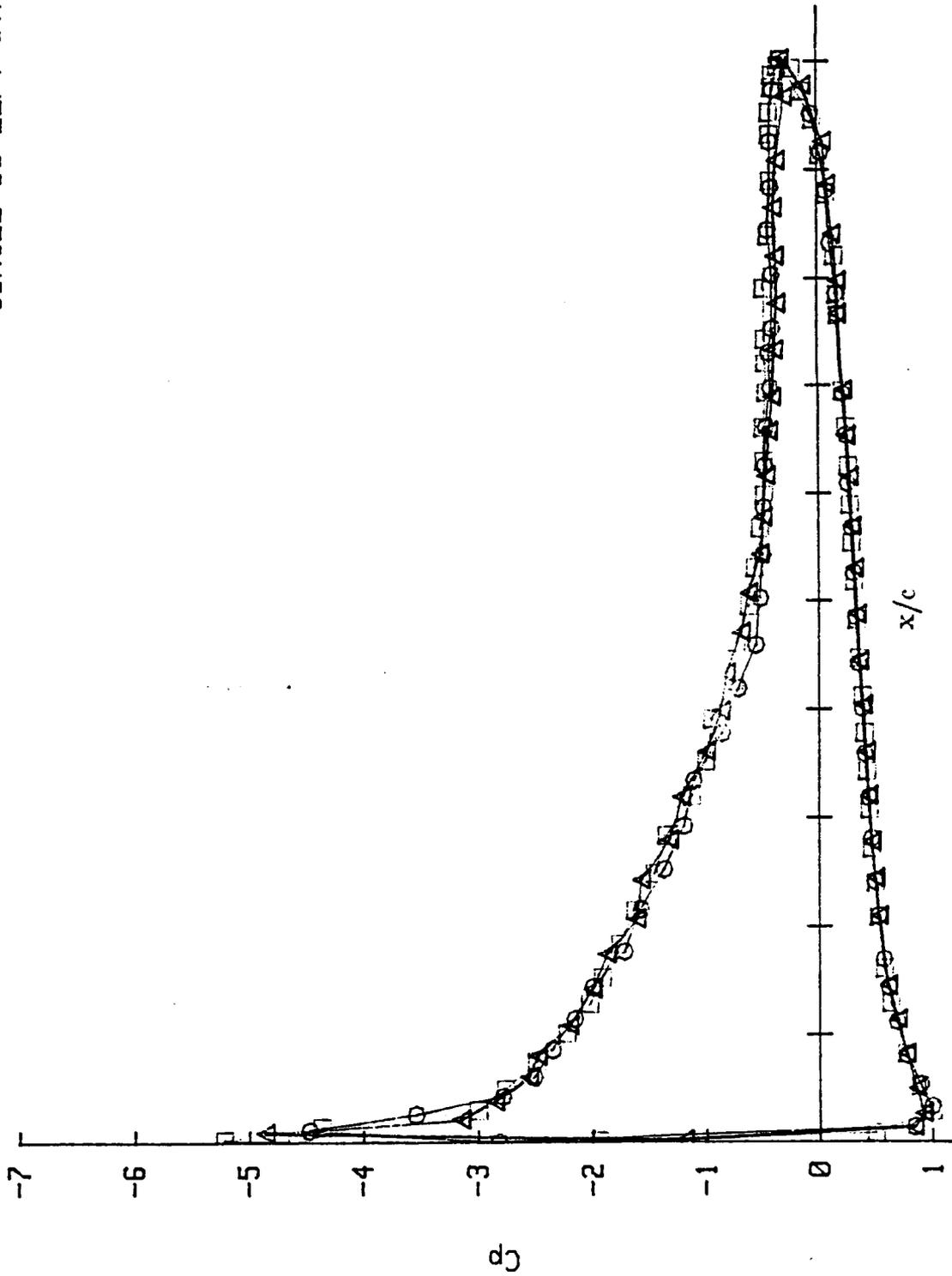
Figure 6f. Airfoil pressure distribution for $Re_c = 1.62 \times 10^6$; $\alpha = 13$ degrees.

32

RUN 28 POST TEST PLOT OF AVERAGE Cp vs. X/C

TRIANGLE IS RIGHT STATION
SQUARE IS MIDDLE STATION
CIRCLE IS LEFT STATION
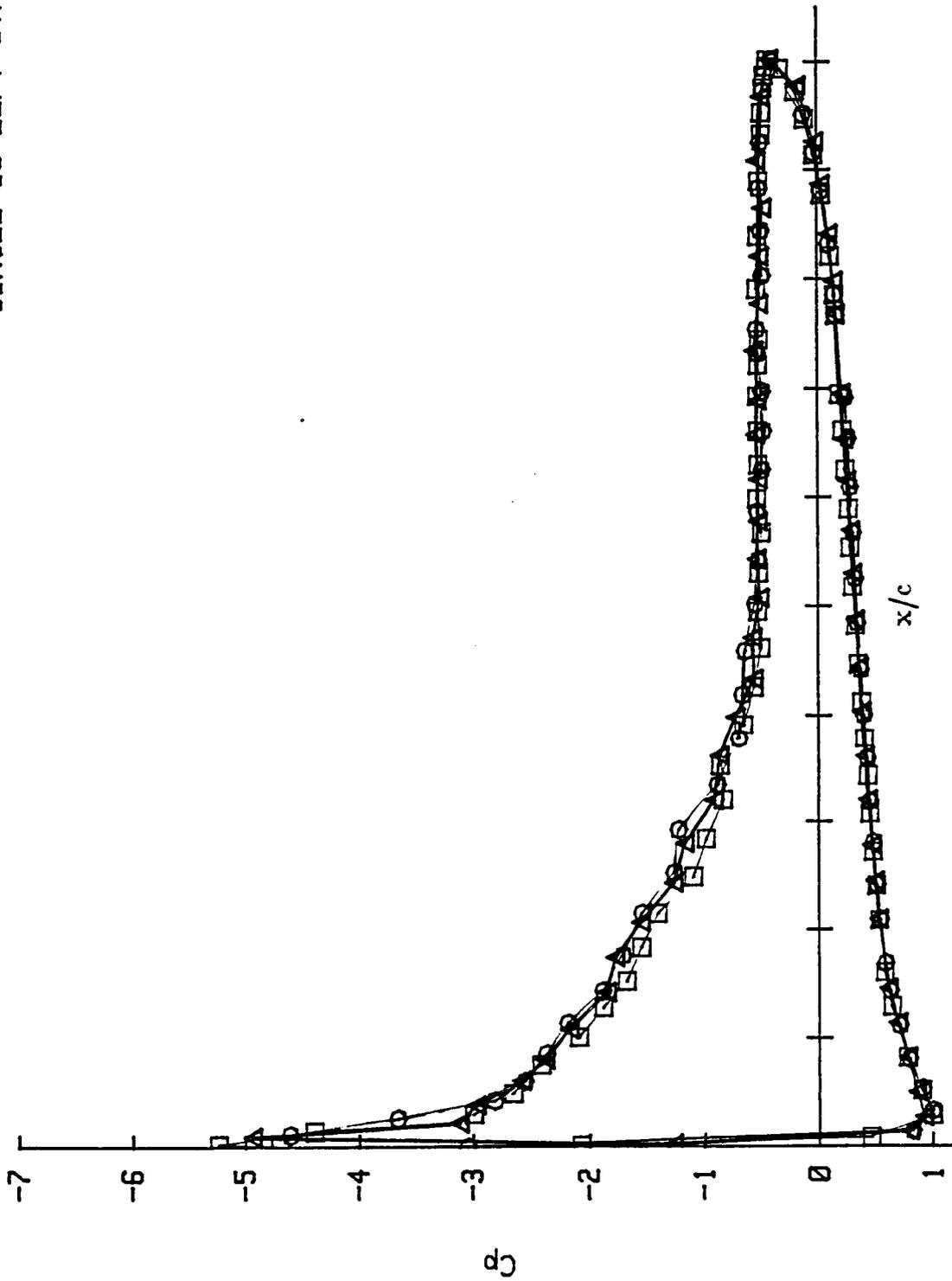
Figure 6g. Airfoil pressure distribution for $Re_c = 1.60 \times 10^6$; $\alpha = 14$ degrees.

33

RUN 30 POST TEST PLOT OF AVERAGE Cp vs. X/C

TRIANGLE IS RIGHT STATION
SQUARE IS MIDDLE STATION
CIRCLE IS LEFT STATION
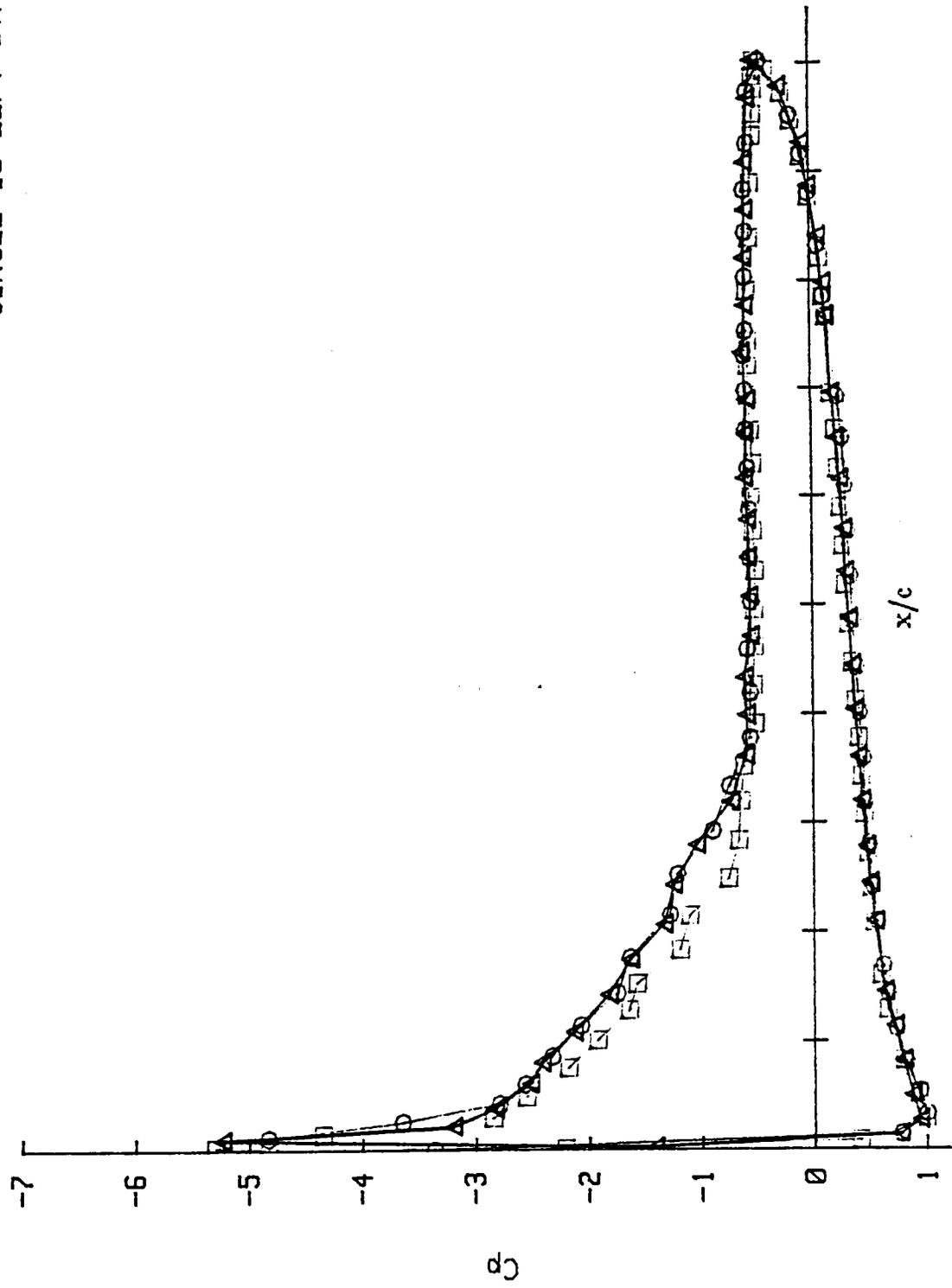
Figure 6h. Airfoil pressure distribution for $Re_c = 1.58 \times 10^6$; $\alpha = 15$ degrees.

34

Figure 6i. Airfoil pressure distribution for $Re_c = 1.70 \times 10^6$; $\alpha = 16$ degrees.

35

Figure 6j. Airfoil pressure distribution for $Re_c = 1.70 \times 10^6$; $\alpha=13$ degrees.

36
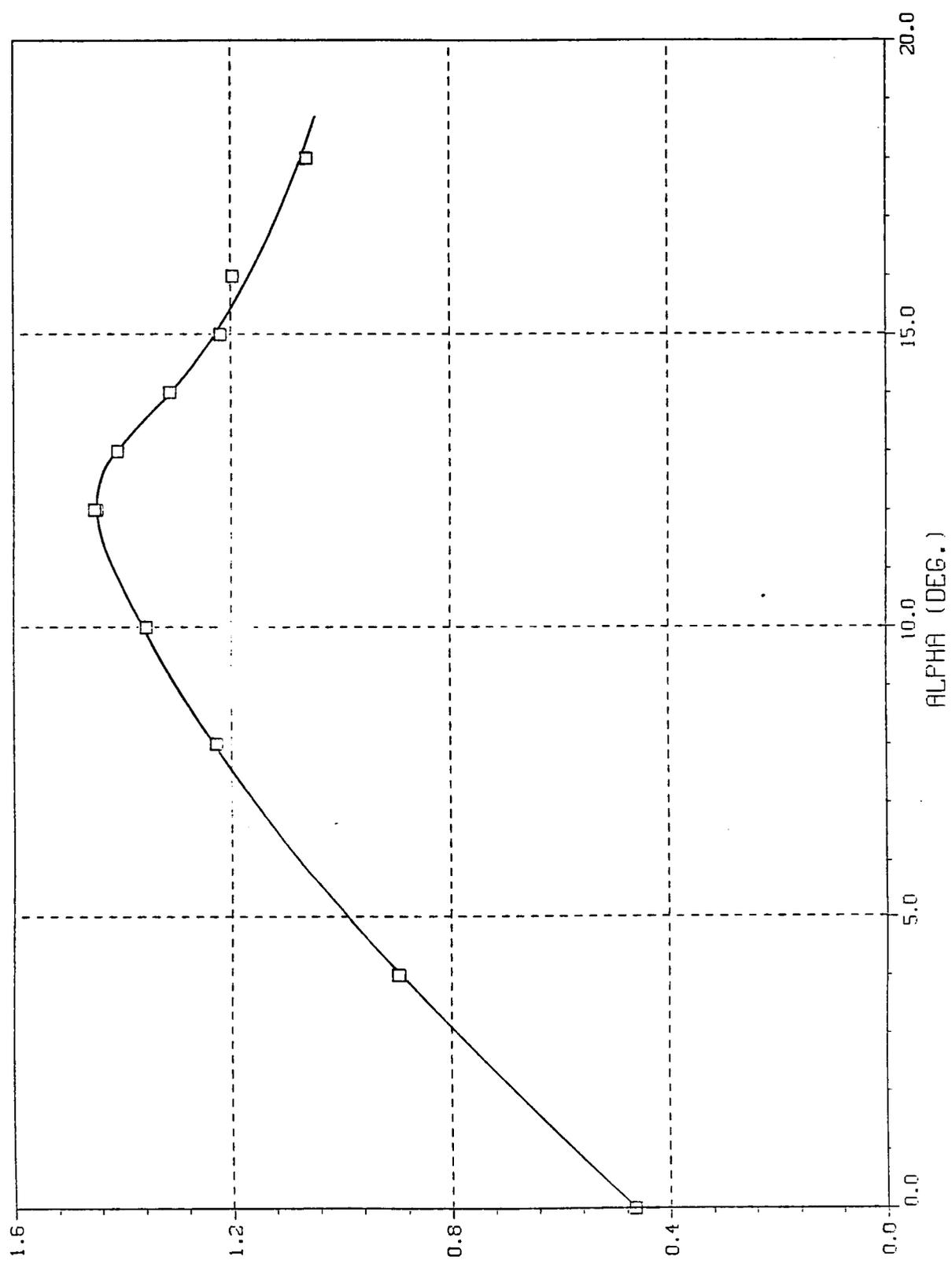
Figure 7a. Airfoil section characteristics for $Re_c = 1.64 \times 10^6$; C_L - α
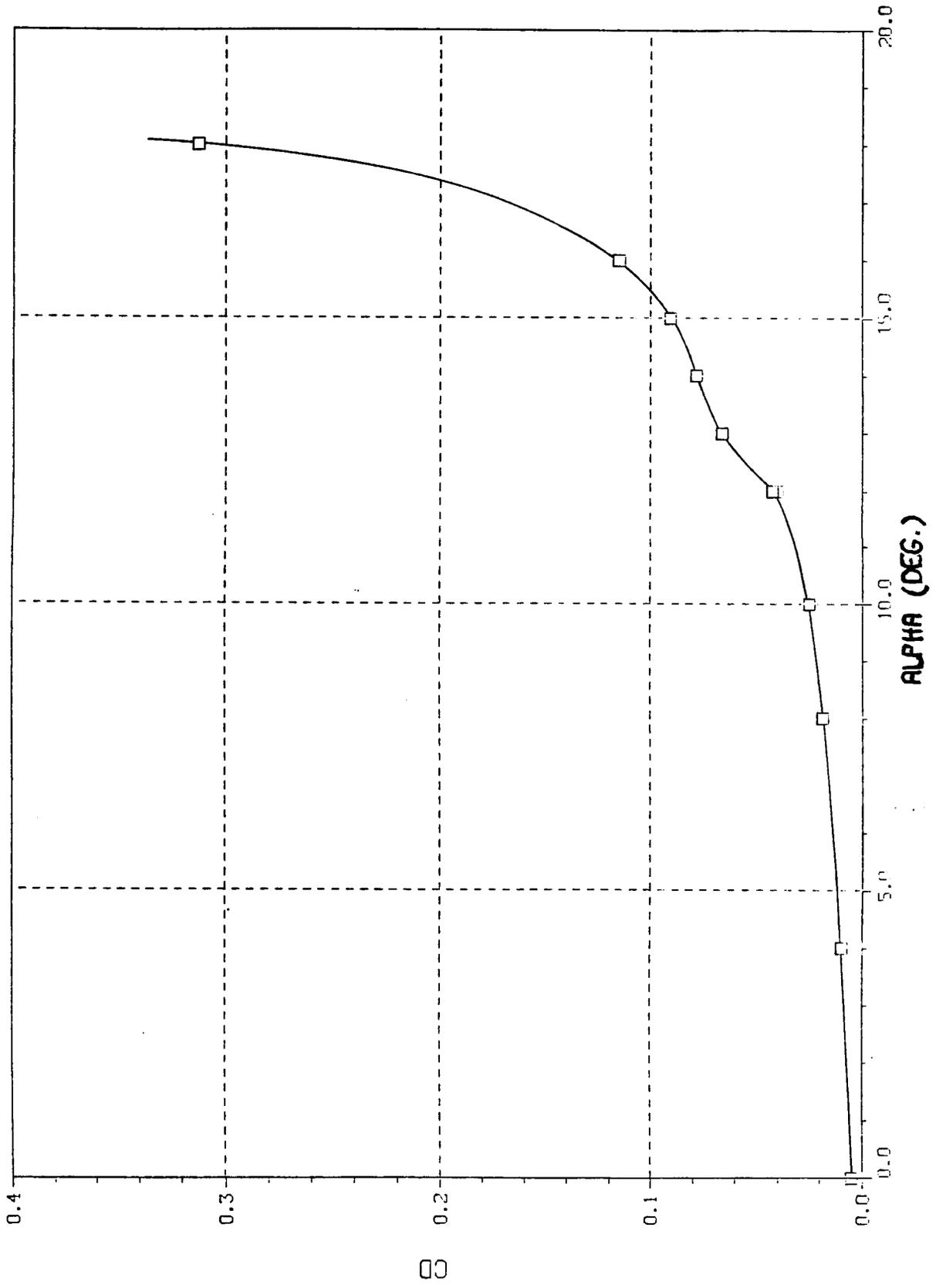
Figure 7b. Airfoil section characteristics for $Re_c = 1.64 \times 10^6$; C_D - α
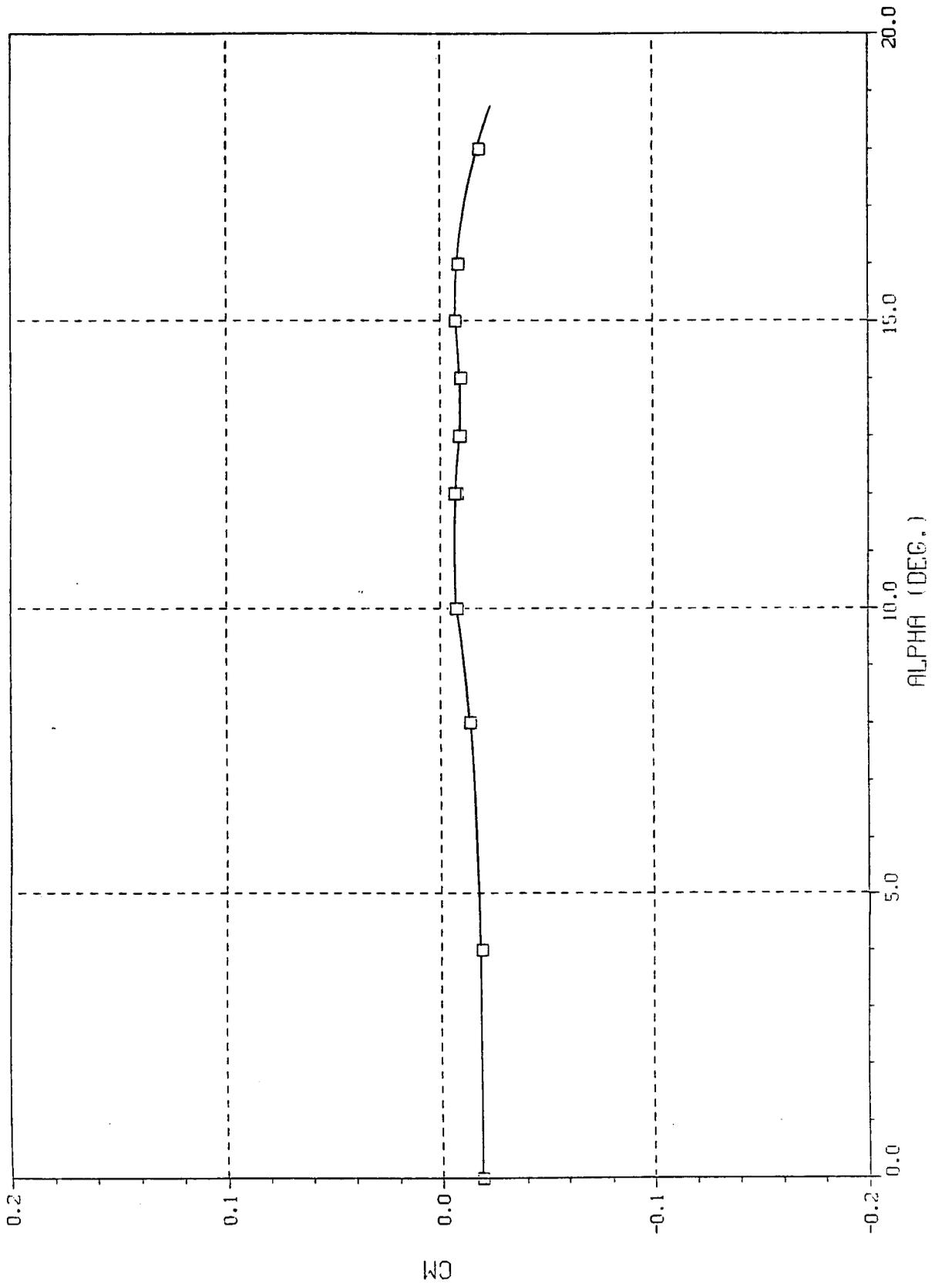
Figure 7c. Airfoil section characteristics for $Re_c = 1.64 \times 10^6$; C_M - α

RUN 101. POST-TEST PLOT OF AVERAGE C_P vs X/C.
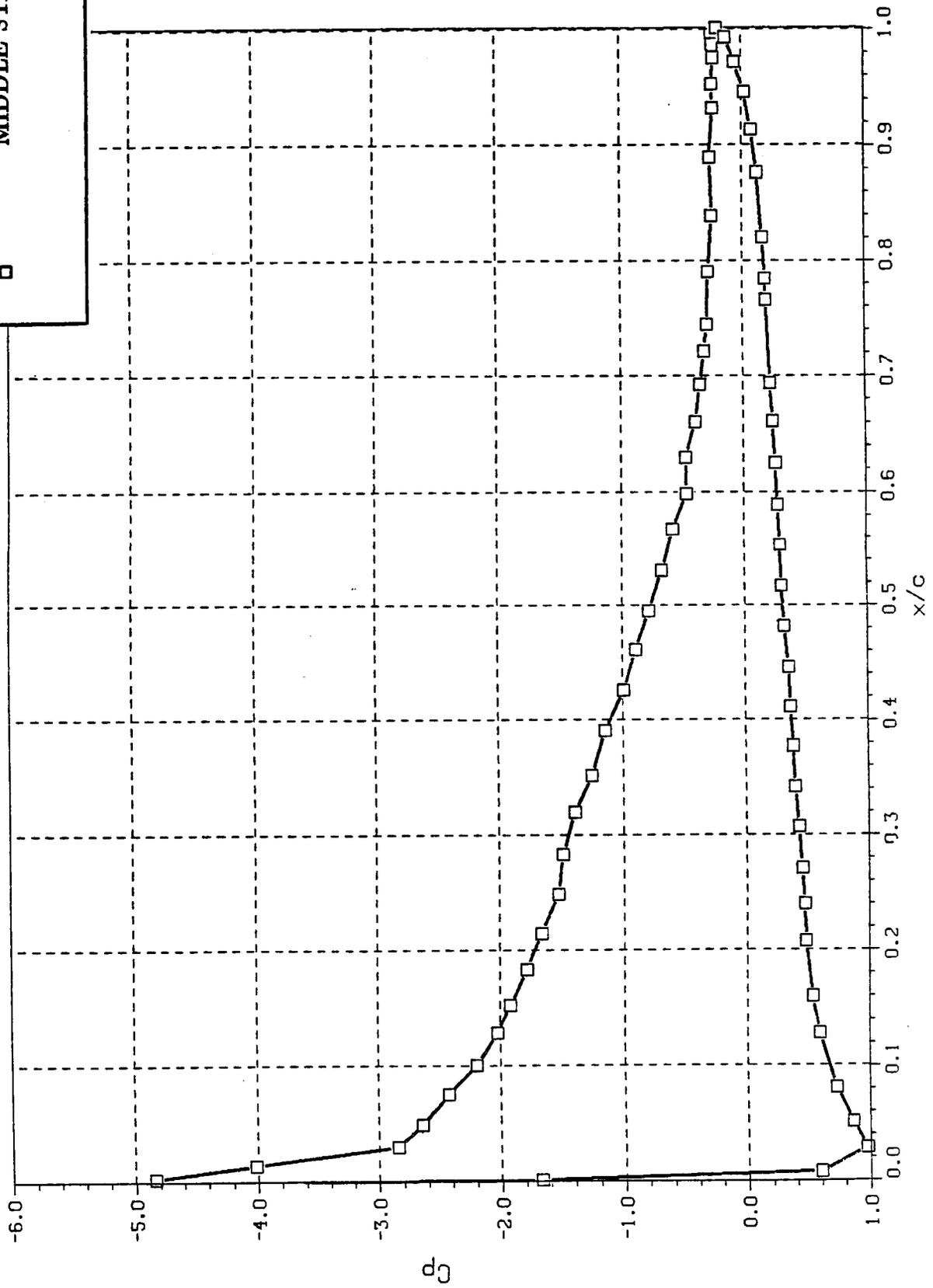
Figure 8. Airfoil pressure distribution for $\alpha = 12$ degrees, $Re_c = 1.21 \times 10^6$.

TRIANGLE IS RIGHT STATION
SQUARE IS MIDDLE STATION
CIRCLE IS LEFT STATION

RUN 76 POST TEST PLOT OF AVERAGE Cp vs. X/C
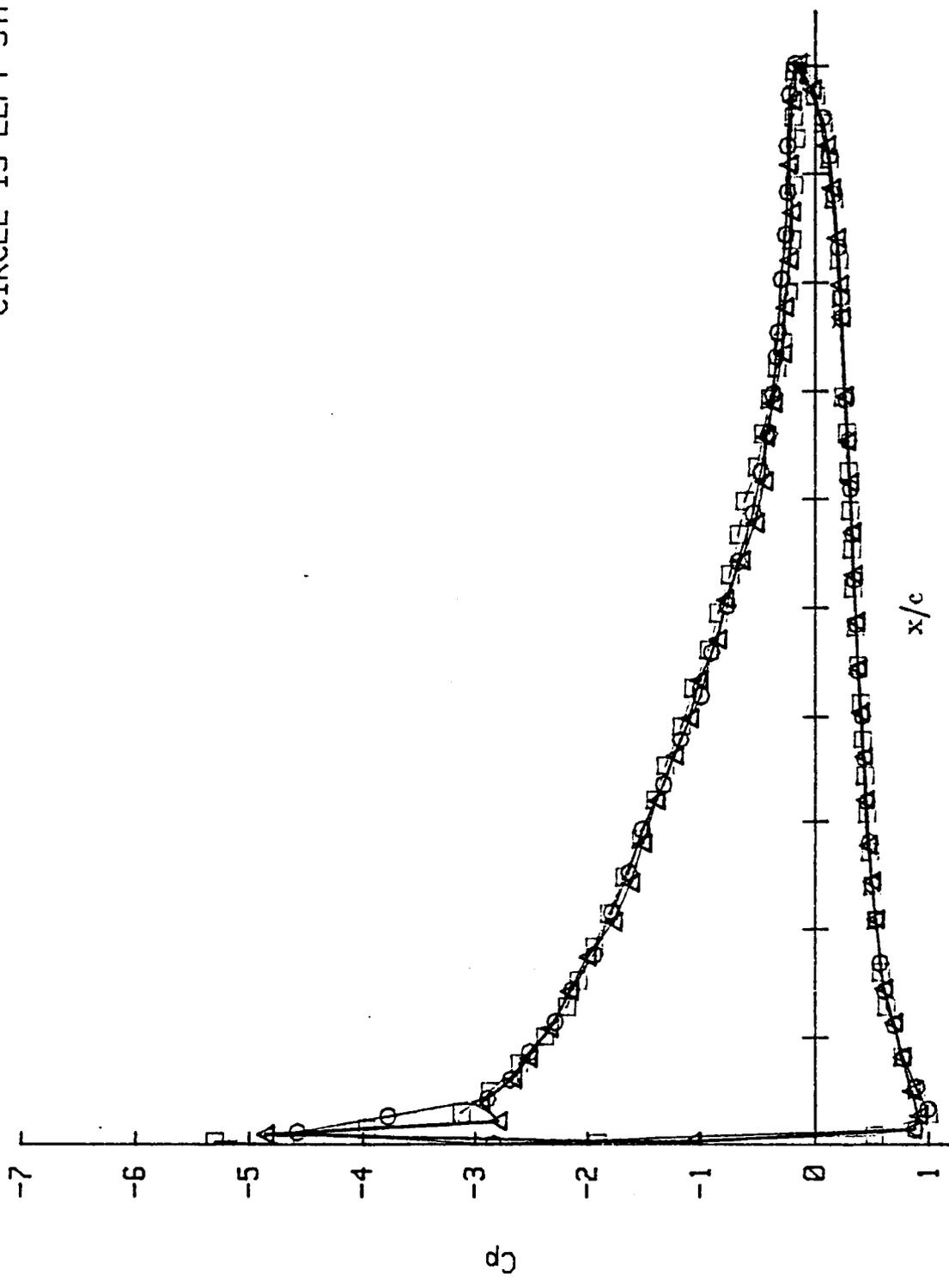
Figure 9. Airfoil pressure distribution for $\alpha = 12$ degrees, $Re_c = 2.31 \times 10^6$.
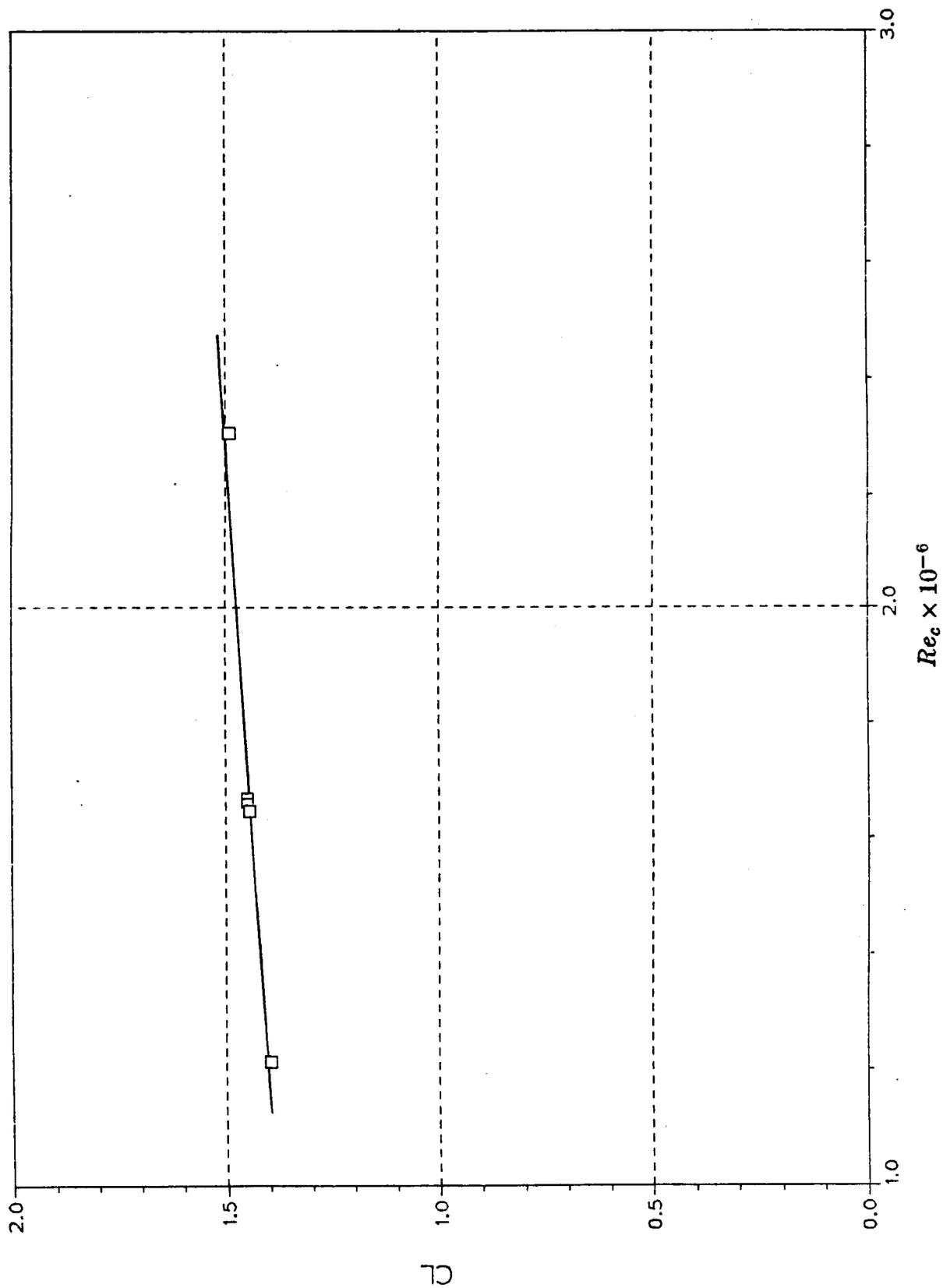
Figure 10a. Variation in C_L with Reynolds number at $\alpha=12$ degrees.

42
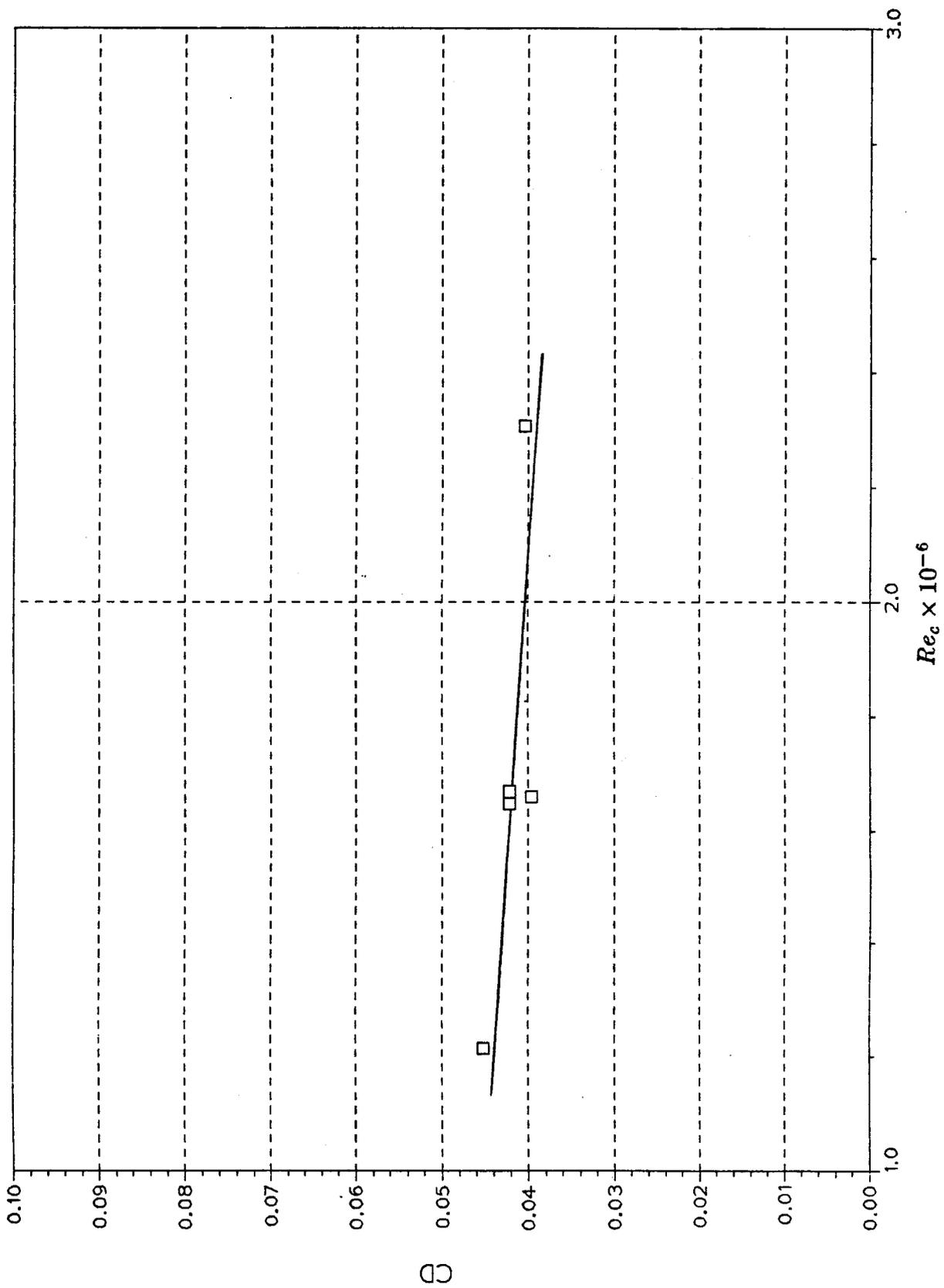
Figure 10b. Variation in C_D with Reynolds number at $\alpha=12$ degrees.
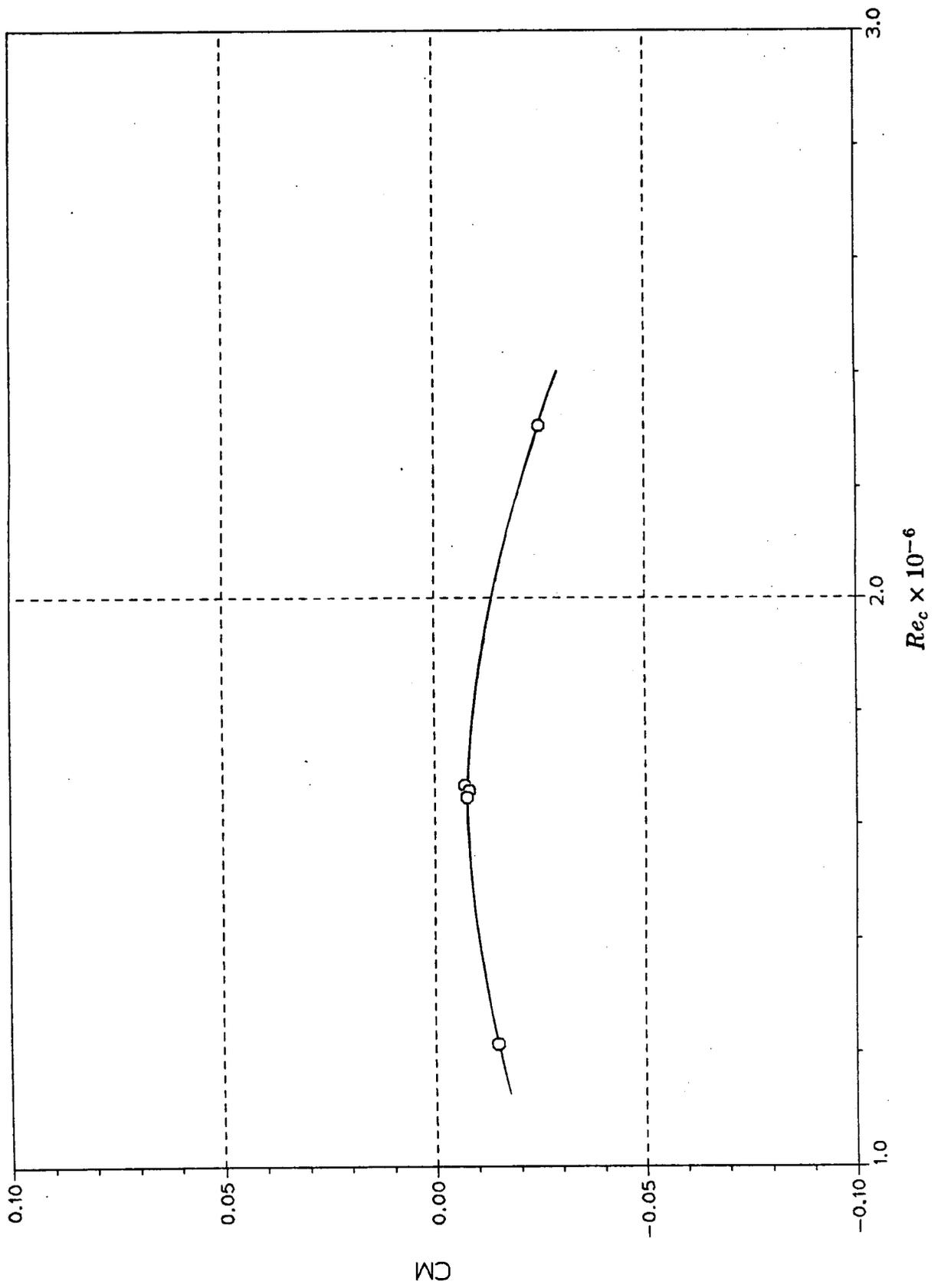
Figure 10c. Variation in C_M with Reynolds number at $\alpha=12$ degrees.
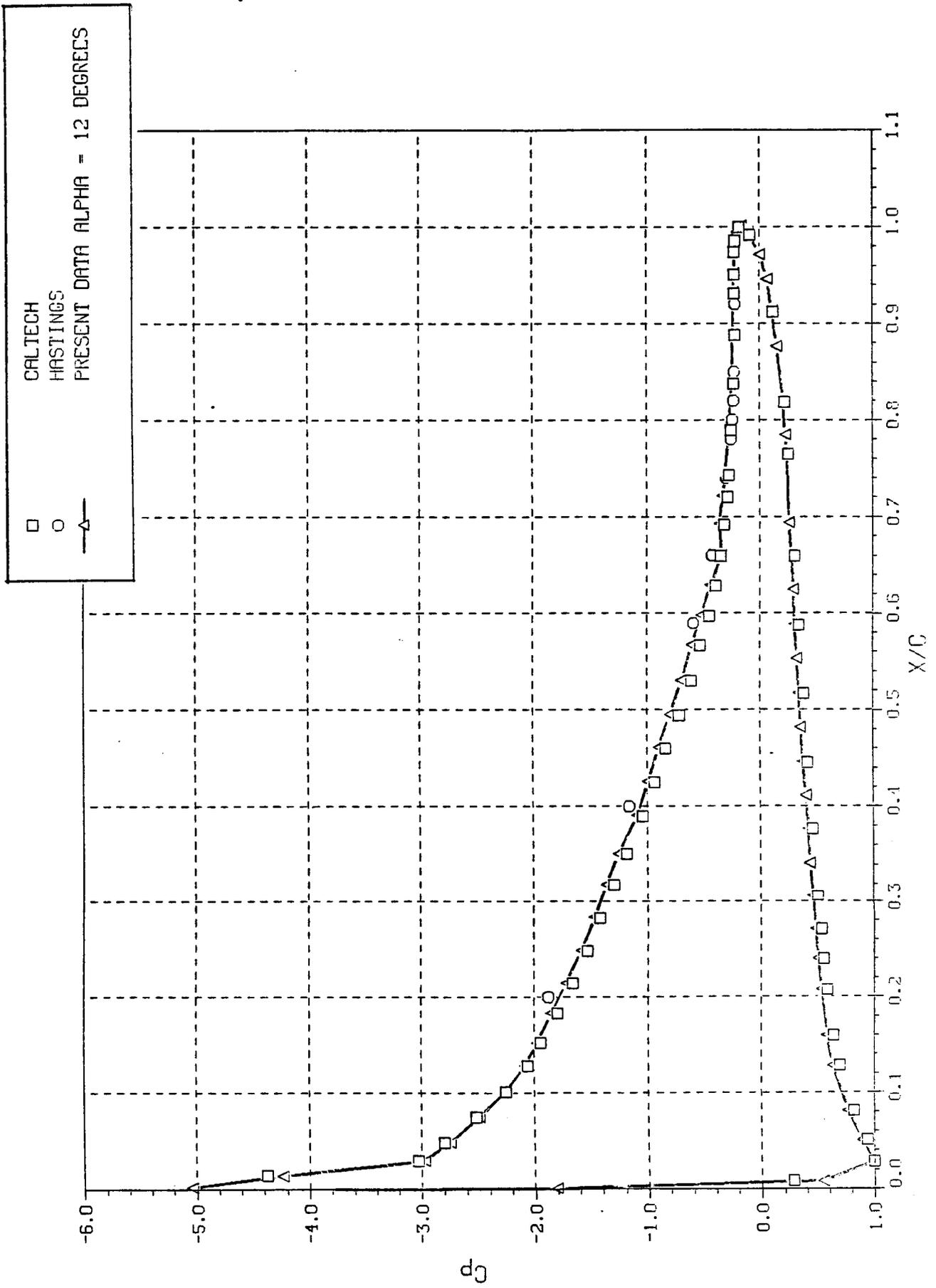
Figure 11. Comparison between measured airfoil pressure distribution of

Hastings *et al* (References 6 and 7), Coles and Wadcock (Reference 5), and present data.
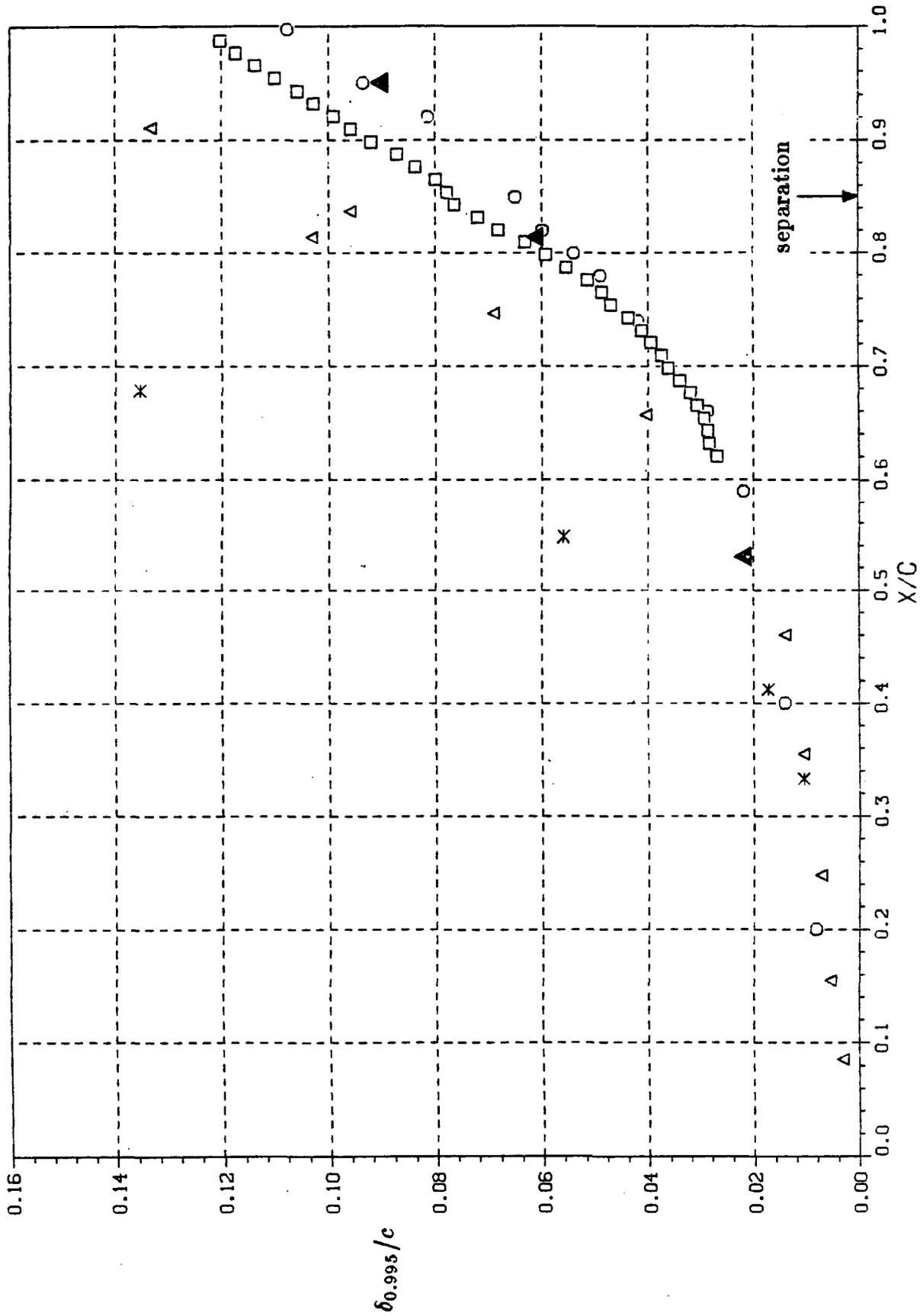
Figure 12a. Measurements of boundary layer thickness, $\delta_{0.995}$.
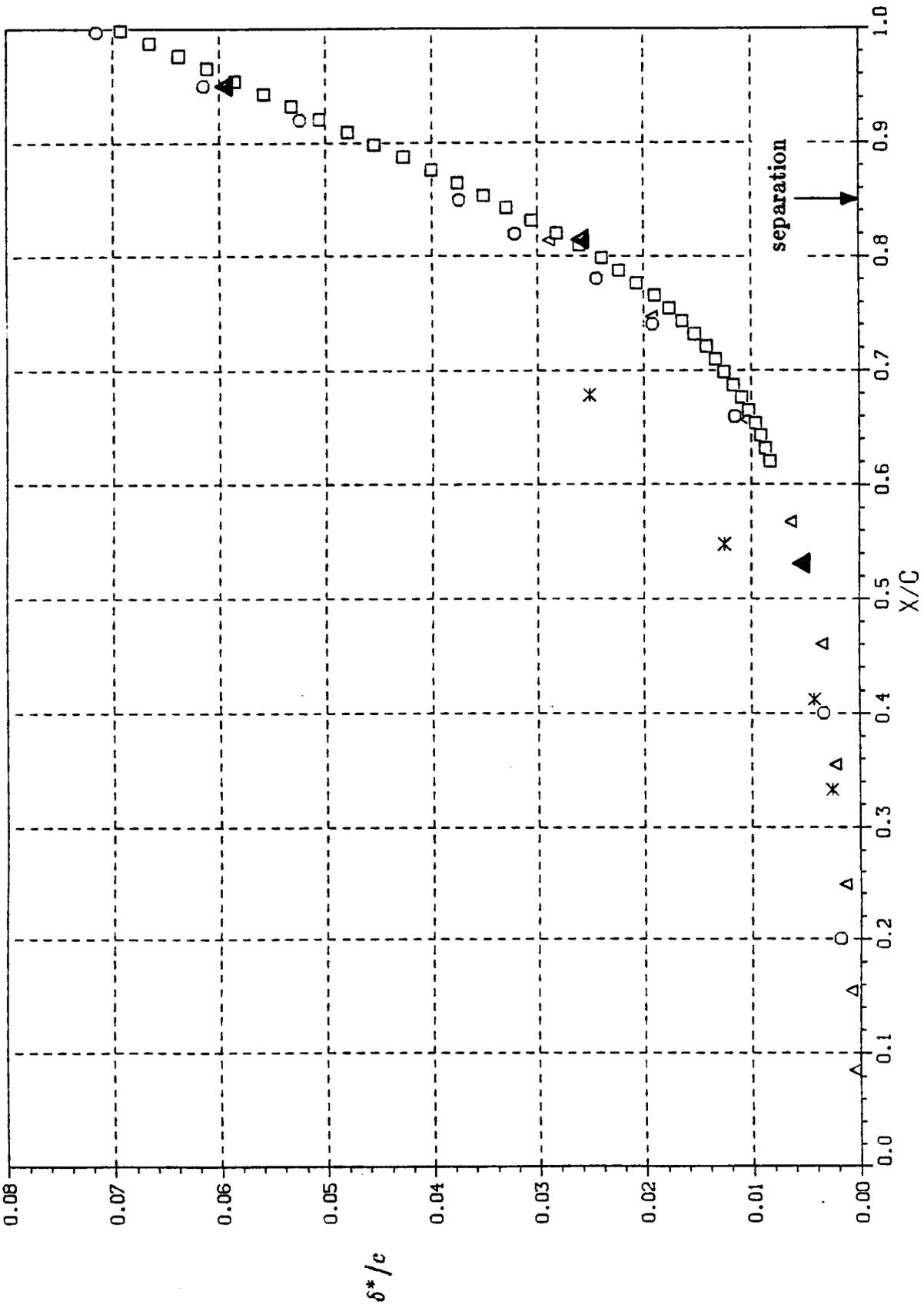
Figure 12b. Measurements of boundary layer displacement thickness, δ^*.

47
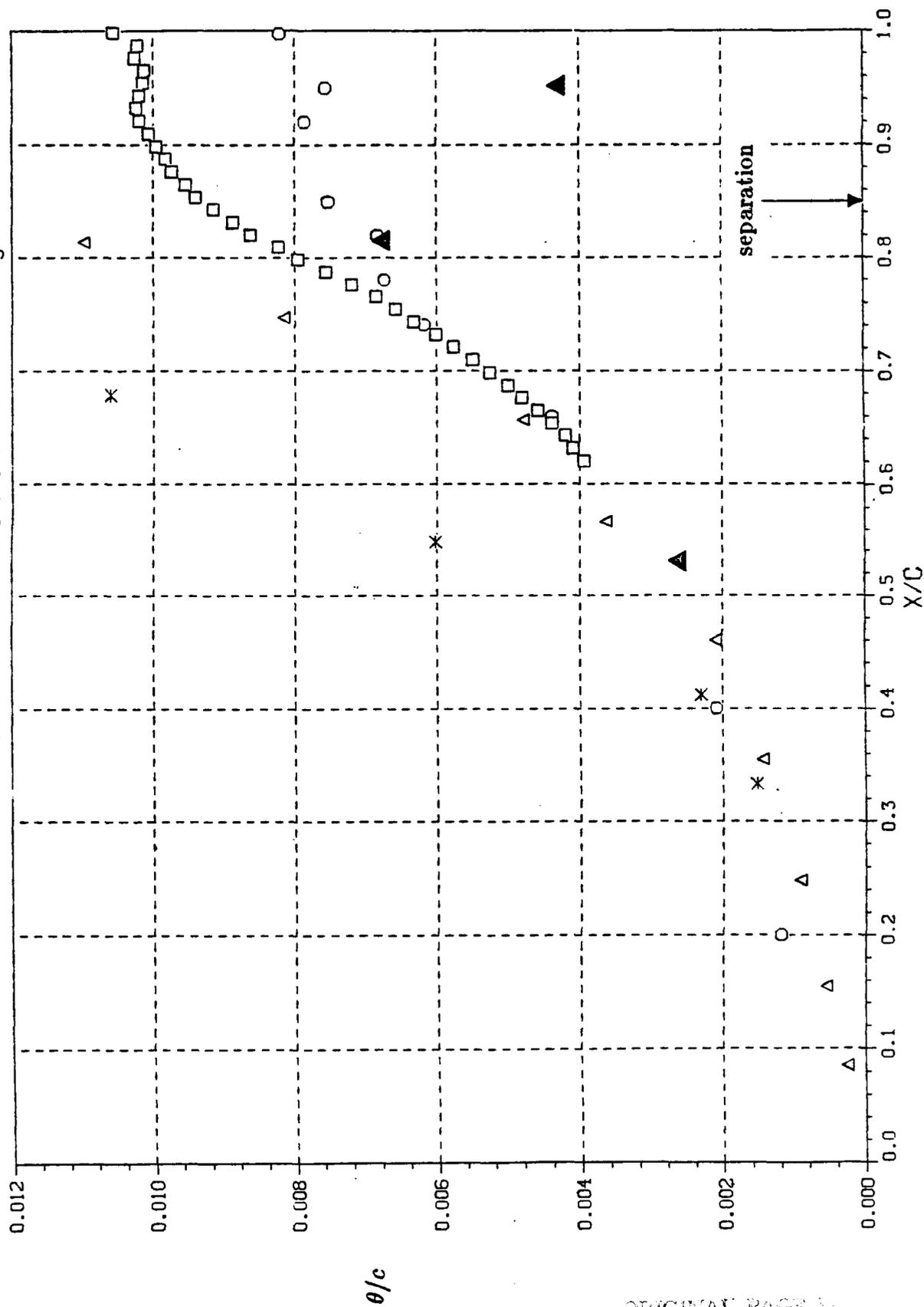
Figure 12c. Measurements of boundary layer momentum thickness, θ.
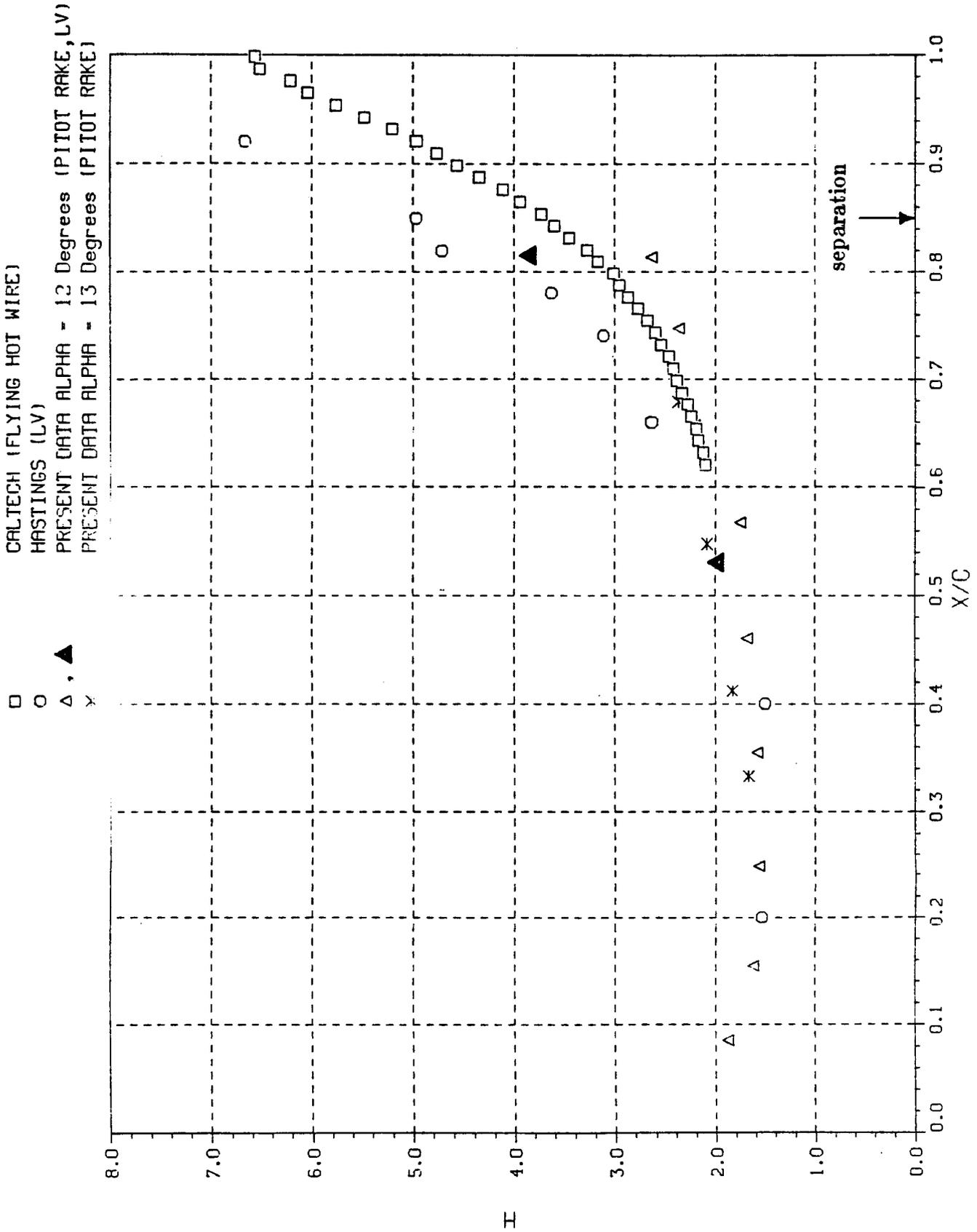
Figure 12d. Measurements of boundary layer shape factor, $H = \delta^*/\theta$.
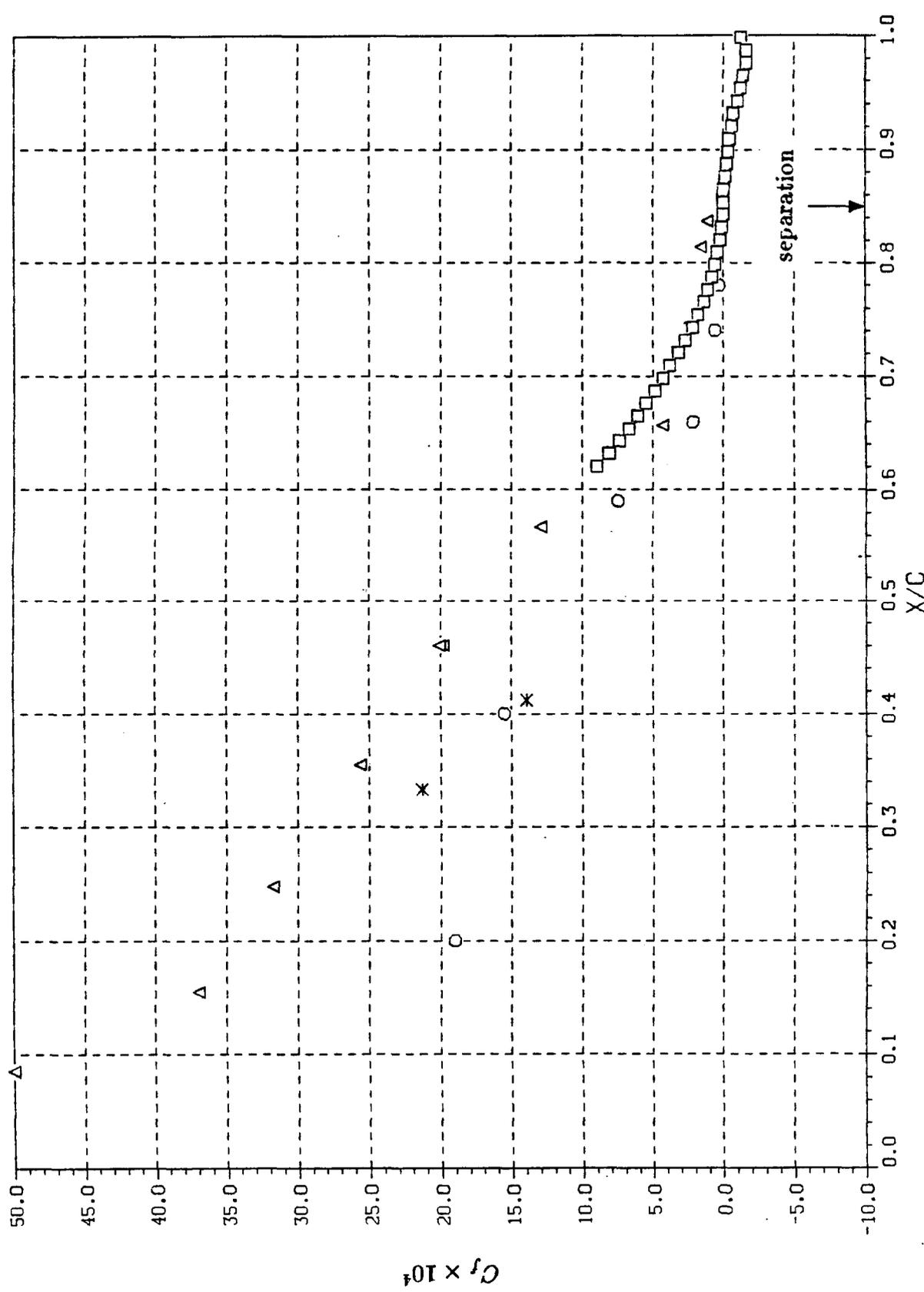
Figure 13. Local skin friction coefficient estimated from Clauser plot of mean velocity.
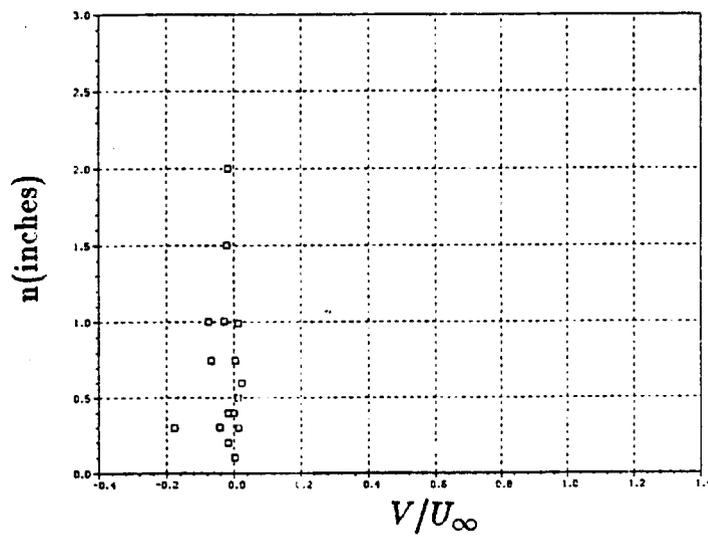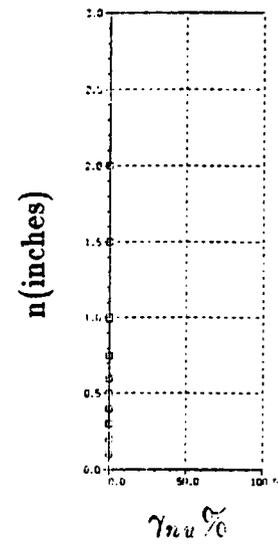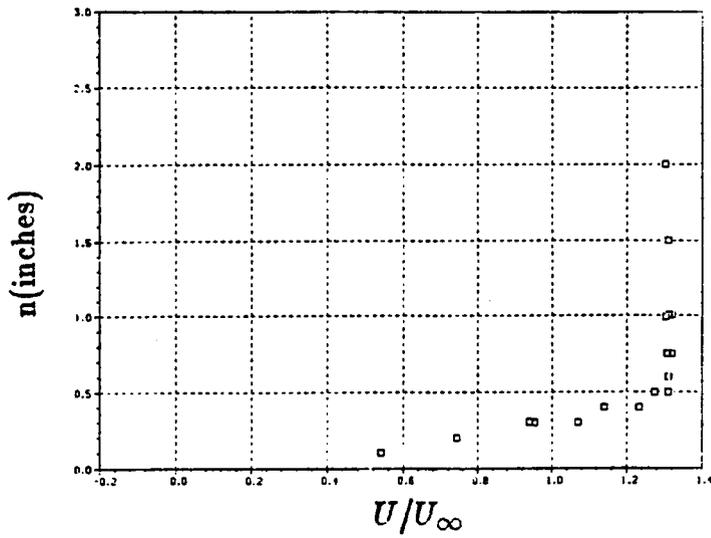
ORIGINAL PAGE IS
OF POOR QUALITY
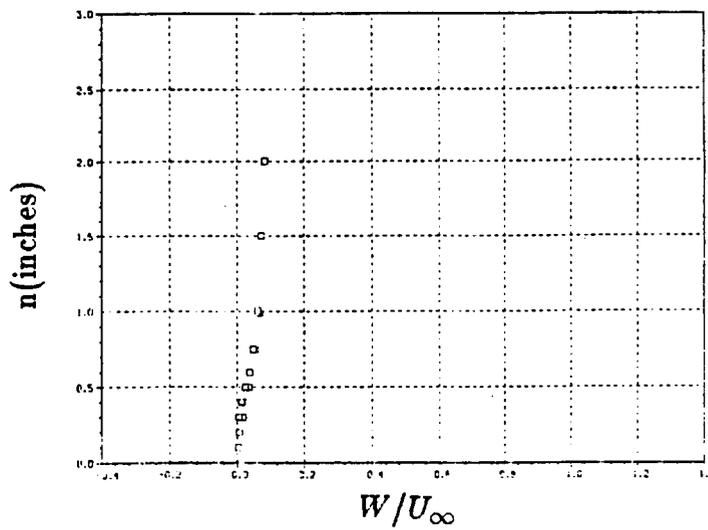
Figure 14a. LV measurements in the boundary layer at x/c=0.529.

Measurements of mean velocity.
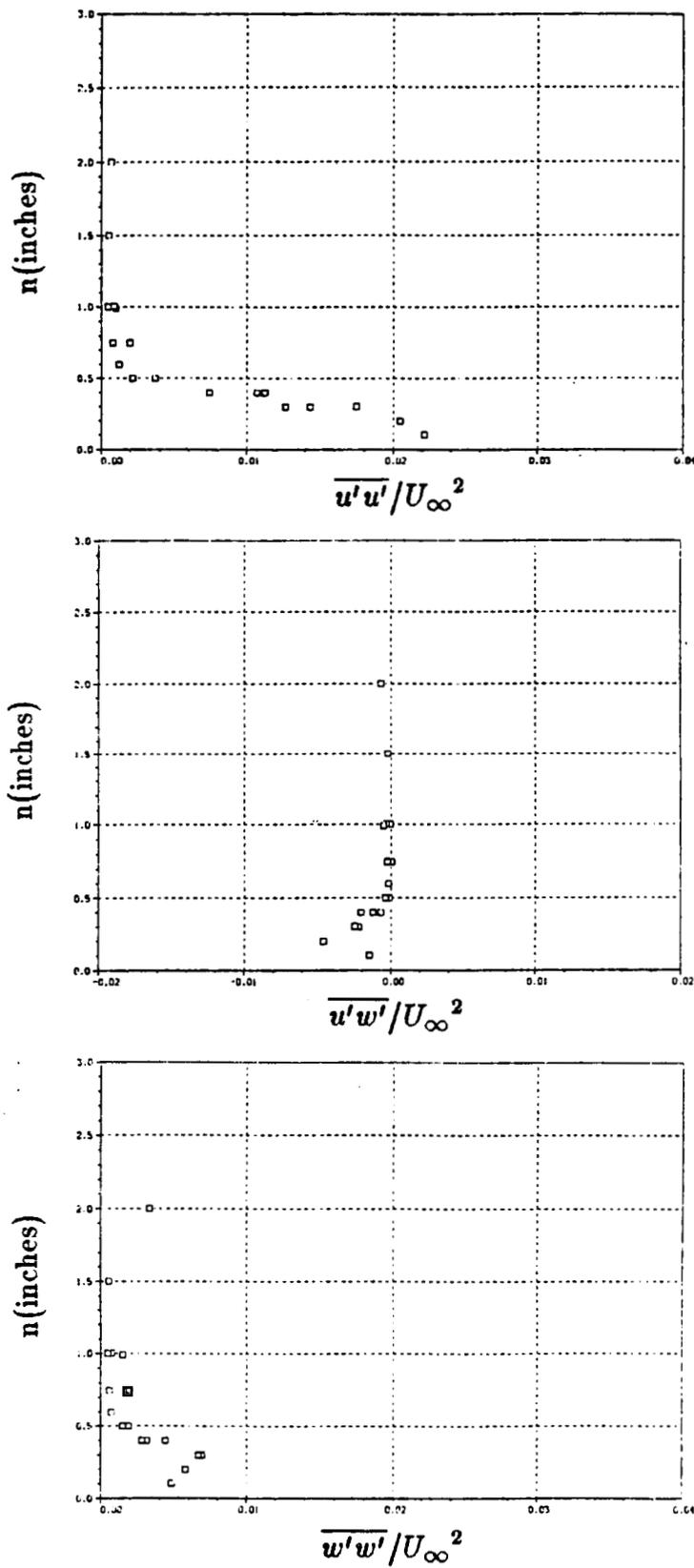
Figure 14b. LV measurements in the boundary layer at x/c=0.529.

Turbulence measurements.
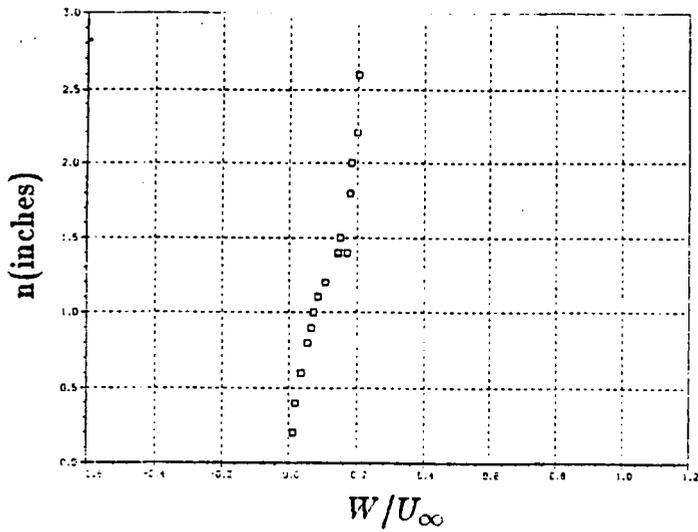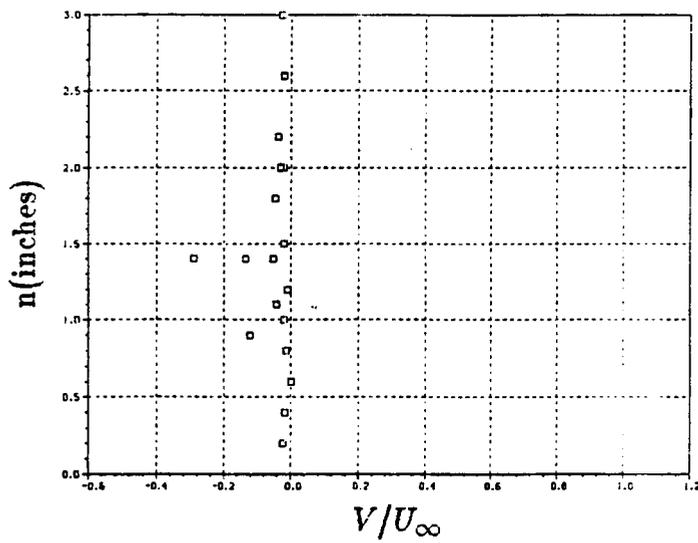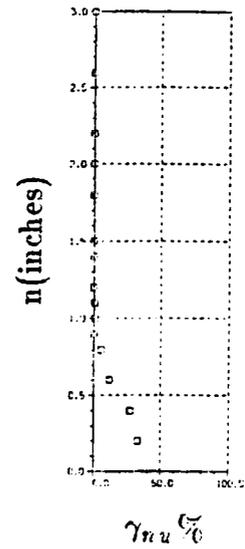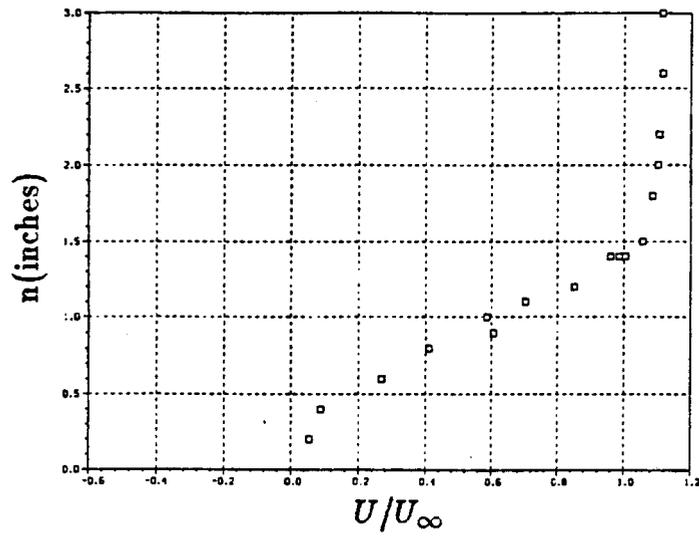
ORIGINAL PAGE IS
OF POOR QUALITY

Figure 15a. LV measurements in the boundary layer at x/c =0.815.

Measurements of mean velocity.
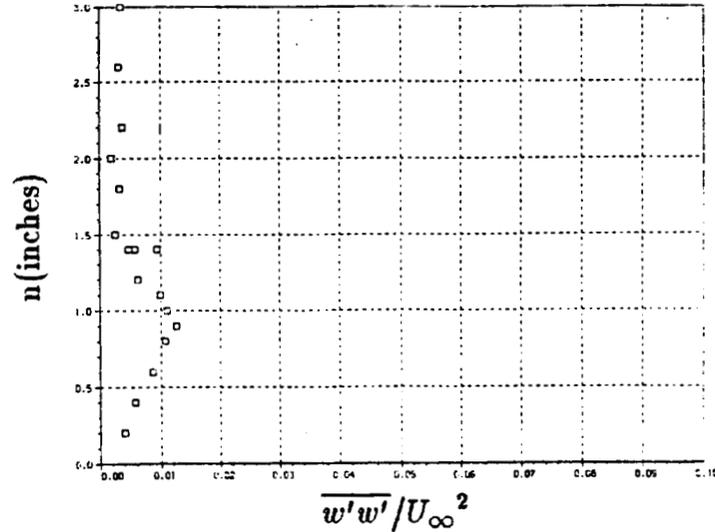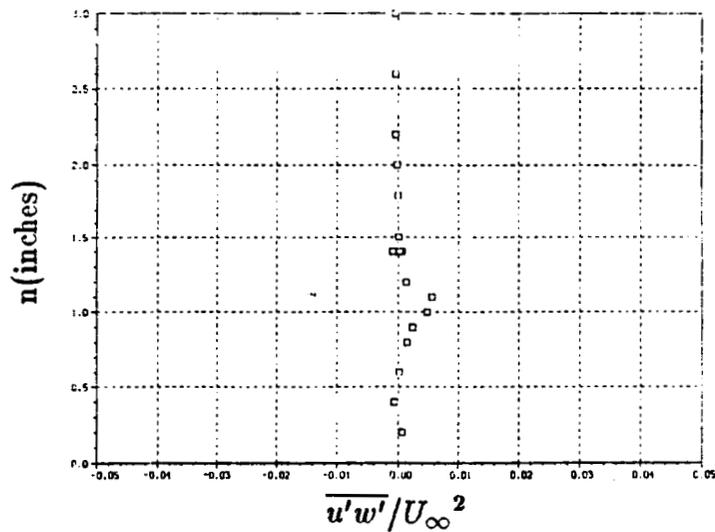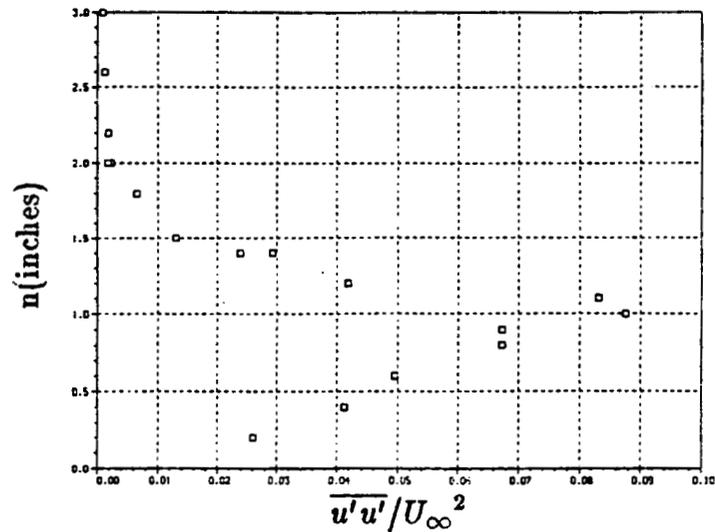
Figure 15b. LV measurements in the boundary layer at x/c =0.815.

Turbulence measurements.
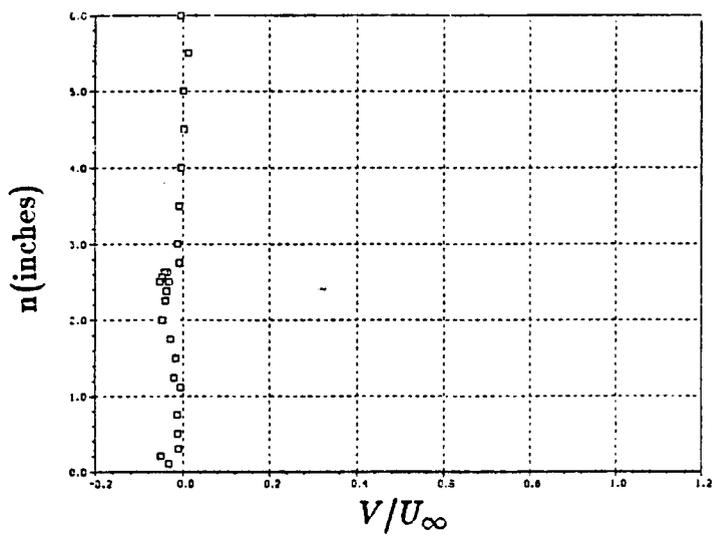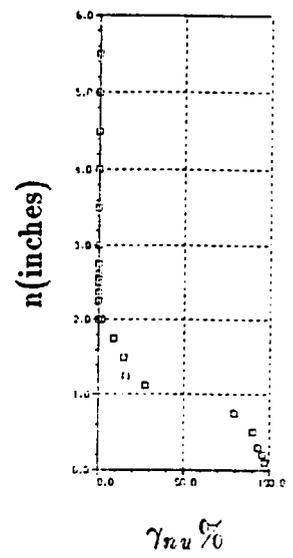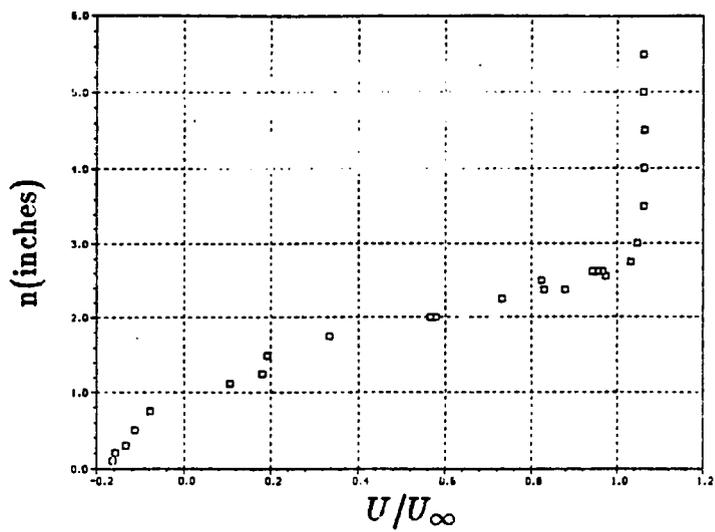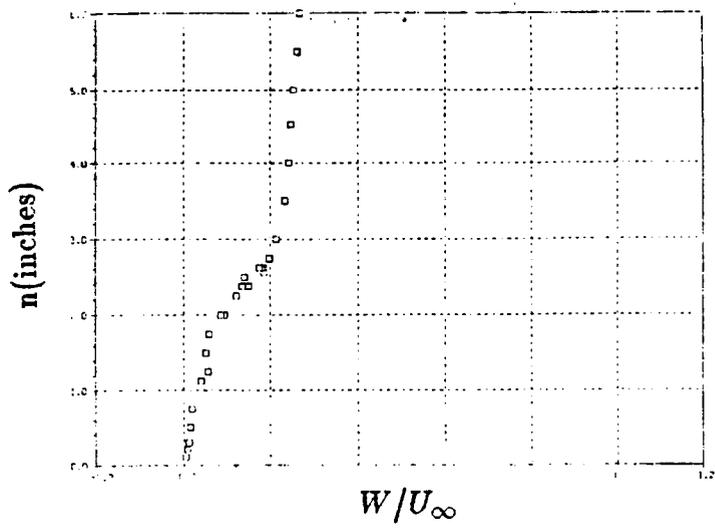
Figure 16a. LV measurements in the boundary layer at x/c =0.952.

Measurements of mean velocity.
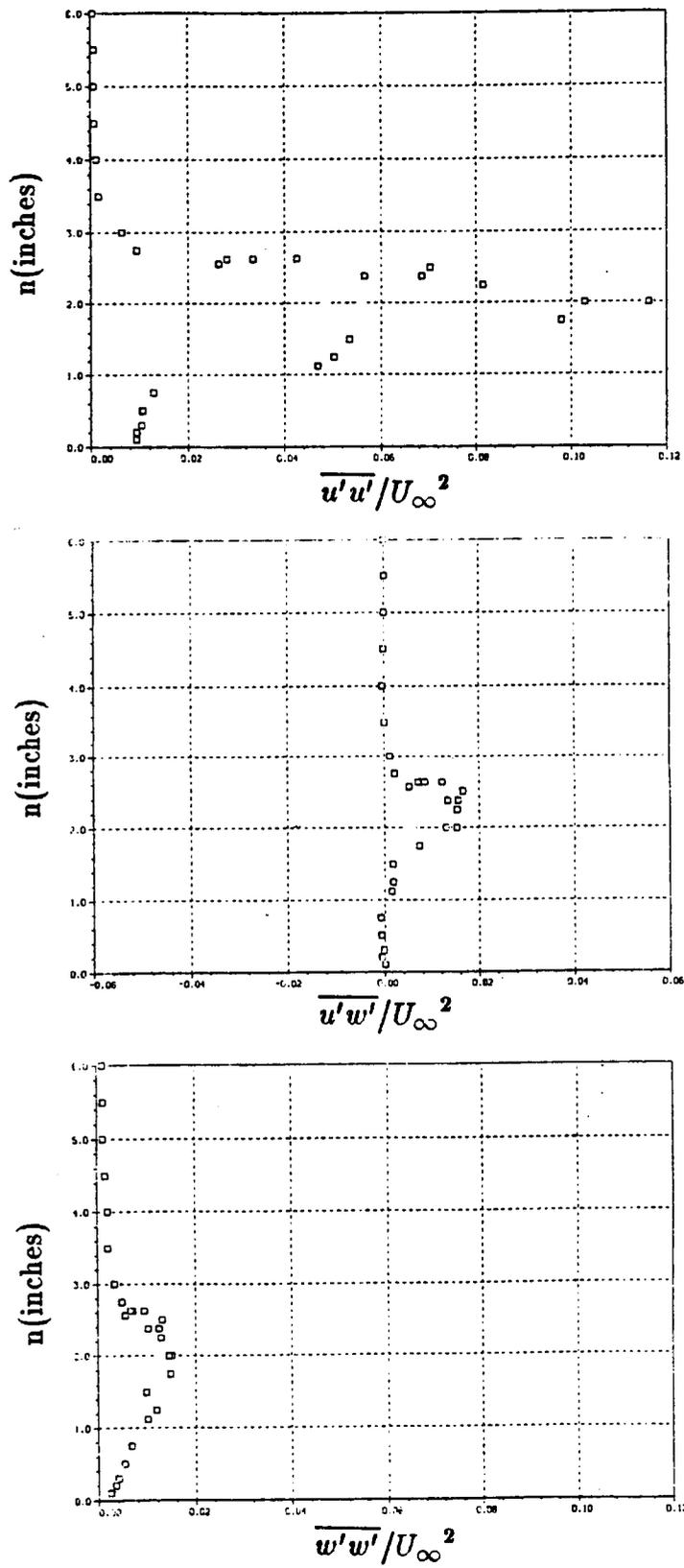
Figure 16b. LV measurements in the boundary layer at x/c =0.952.

Turbulence measurements.
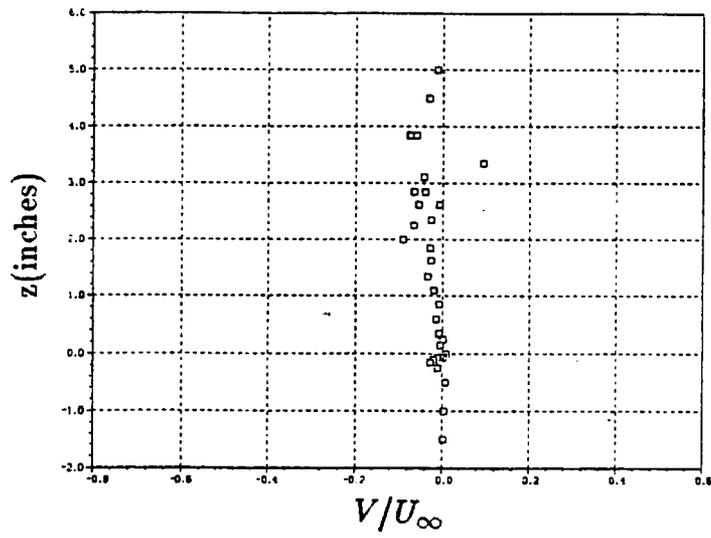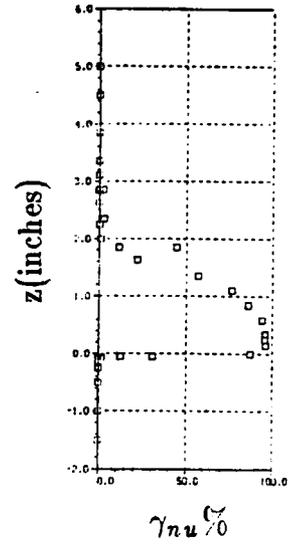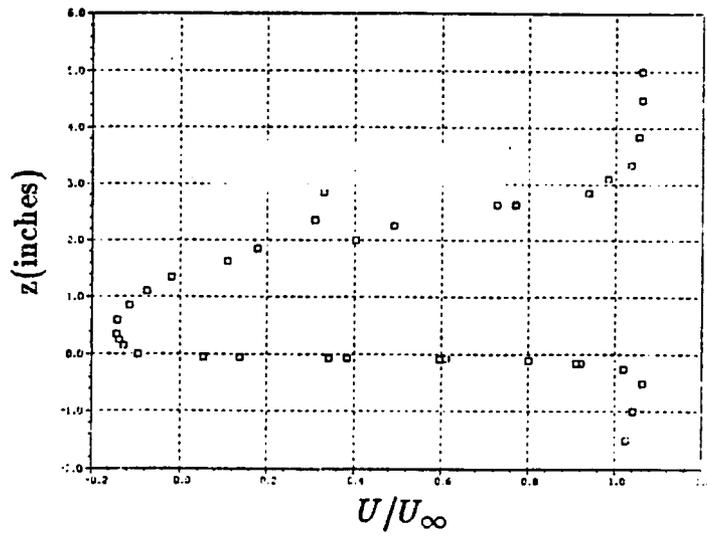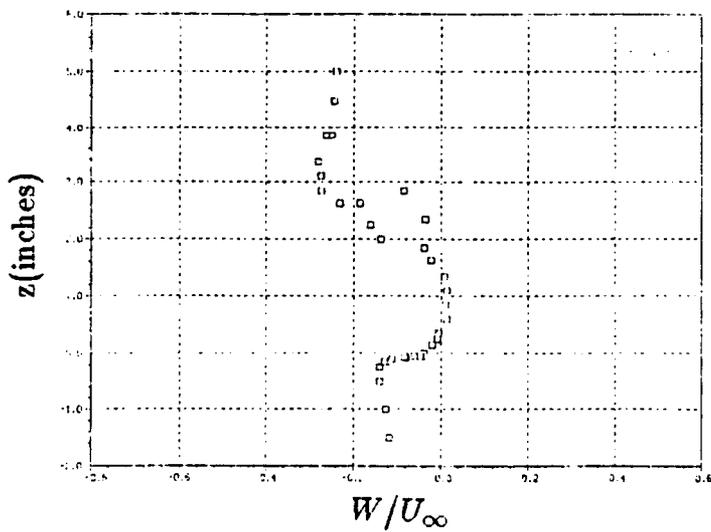
Figure 17a. LV measurements in the wake at $x_w/c = 0.007$.

Measurements of mean velocity.

Figure 17b. LV measurements in the wake at $x_w/c = 0.007$.

Turbulence measurements.
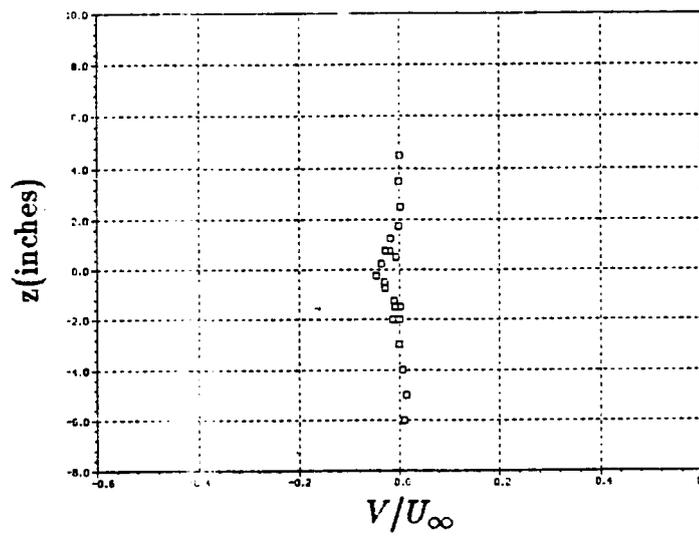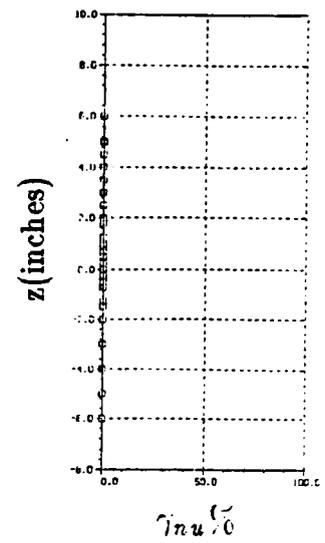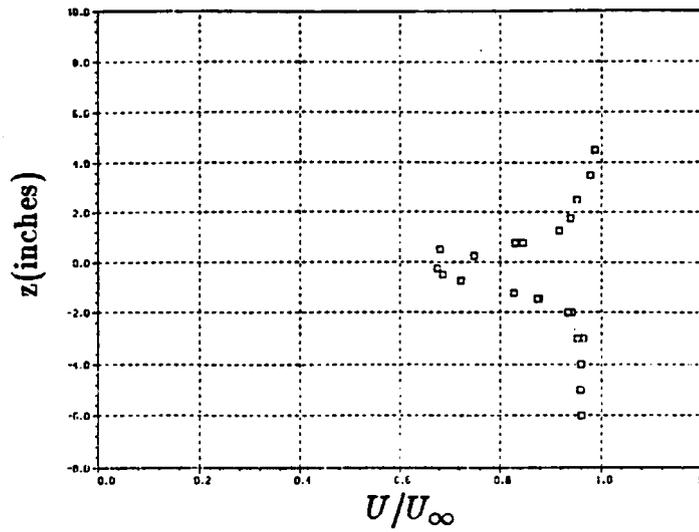
Figure 18a. LV measurements in the wake at x_w/c =0.282.
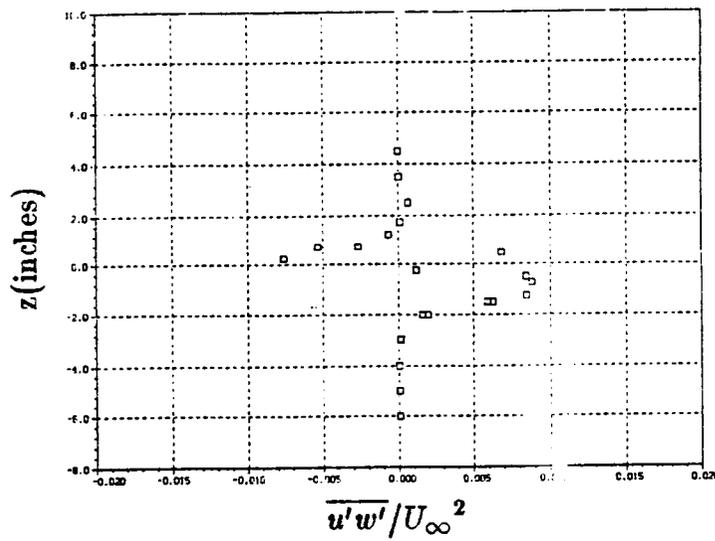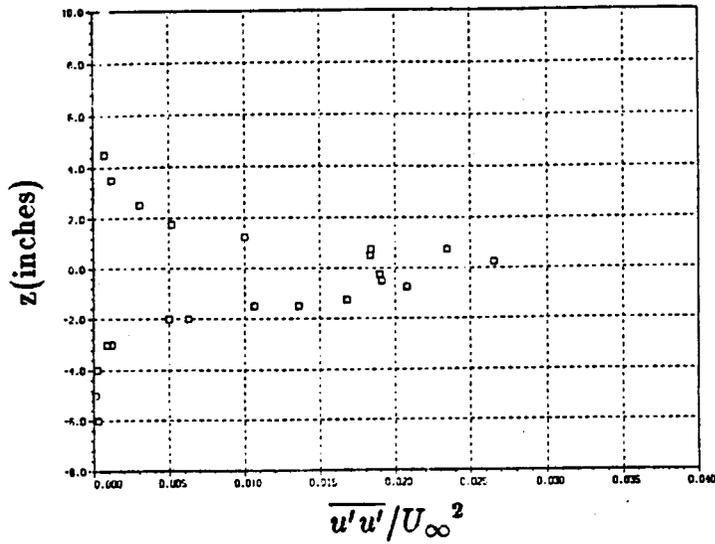
Measurements of mean velocity.

Figure 18b. LV measurements in the wake at $x_w/c = 0.282$.

Turbulence measurements.

NASA	**Report Documentation Page**	
National Aeronautics and Space Administration		

1. Report No.	2. Government Accession No.	3. Recipient's Catalog No.
NASA CR 177450		

4. Title and Subtitle	5. Report Date
Investigation of Low-Speed Turbulent Separated Flow Around Airfoils	August 1987
	6. Performing Organization Code

7. Author(s)	8. Performing Organization Report No.
Alan J. Wadcock Analytical Methods, Inc. Redmond, WA	
	10. Work Unit No.
	505-60-11

9. Performing Organization Name and Address	11. Contract or Grant No.
NASA Ames Research Center Moffett Field, CA 94035	NAS2-11601
	13. Type of Report and Period Covered

12. Sponsoring Agency Name and Address	Contractor Report
National Aeronautics and Space Administration Washington, D.C. 20546	14. Sponsoring Agency Code

15. Supplementary Notes

Point of Contact: L. A. Meyn, Ames Research Center, M.S. 247-2
Moffett Field, CA 94035
(415) 694-5038 or FTS 464-5038

16. Abstract

The present report documents a low-speed wind tunnel experiment to measure the flowfield around a two-dimensional airfoil operating close to maximum lift. Boundary layer separation occurs on the upper surface at $x/c = 0.85$. A three-component laser velocimeter, coupled with a computer-controlled data acquisition system, was used to obtain three orthogonal mean velocity components and three components of the Reynolds stress tensor in both the boundary layer and wake of the airfoil. Pressure distributions on the airfoil, skin friction distribution on the upper surface of the airfoil, and integral properties of the airfoil boundary layer are also documented. In addition to these "near field" flow properties, static pressure distributions, both upstream and downstream from the airfoil and on the walls of the wind tunnel, are also presented.

17. Key Words (Suggested by Author(s))	18. Distribution Statement
Separated Flow, Turbulence, Trailing-edge, 3D Laser Doppler Anemometer, Airfoils, Boundary Layer	Unlimited Subject Category: O2

19. Security Classif. (of this report)	20. Security Classif. (of this page)	21. No. of pages	22. Price
Unclassified	Unclassified	60	

NASA FORM 1626 OCT 86